

Airborne investigation of black carbon interaction with low-level, persistent, mixed-phase clouds in the Arctic summer

5 Marco Zanatta^{1,2}, Stephan Mertes³, Olivier Jourdan⁴, Regis Dupuy⁴, Emma Järvinen², Martin Schnaiter², Oliver Eppers^{5,6},
Johannes Schneider⁵, Zsófia Jurányi¹, Andreas Herber¹

¹Alfred-Wegener-Institut, Helmholtz-Zentrum für Polar- und Meeresforschung (AWI), Bremerhaven, Germany

²Institute of Meteorology and Climate Research, Karlsruhe Institute of Technology, Karlsruhe, Germany

³Leibniz-Institut für Troposphärenforschung, Leipzig, Germany

⁴Laboratoire de Météorologie Physique, Université Clermont Auvergne/OPGC/CNRS, UMR 6016, Clermont-Ferrand, France

10 ⁵Particle Chemistry Department, Max Planck Institute for Chemistry, Mainz, Germany

⁶Institute for Atmospheric Physics, University of Mainz, Mainz, Germany

Correspondence to: Marco Zanatta (marco.zanatta@kit.edu)

Abstract. Aerosol-cloud interaction is considered one of the largest sources of uncertainty in radiative forcing estimations. To
15 better understand the role of black carbon (BC) aerosol as a cloud nucleus and the impact of clouds on its vertical distribution
in the Arctic, we report airborne in-situ measurements of BC particles in the European Arctic near Svalbard during the Arctic
CLOUD Observations Using airborne measurements during polar Day (ACLOUD) campaign held in summer 2017. BC was
measured with a single particle soot photometer on board the research aircraft “Polar 6” from the lowest atmospheric layer up
to approximately 3500 m asl. During in-cloud flight transects, BC particles contained in liquid droplets (BC residuals) were
20 sampled through a counterflow virtual impactor (CVI) inlet. Four flights, conducted in the presence of inside-inversion,
surface-coupled, mixed-phase clouds over sea ice, were selected to address the variability of BC above, below, and within the
cloud layer. First, the increase in size and coating thickness of BC particles from the free troposphere to the cloud-dominated
boundary layer confirmed that ground observations were not representative of upper atmospheric layers. Second, although
only 1% of liquid droplets contained a BC particle, the higher number concentration of BC residuals than BC particles sampled
25 below-cloud indicated that the totality of below-cloud BC was activated by nucleation scavenging, but also that alternative
scavenging processes such as activation of free-tropospheric BC at the cloud top might occur. Third, the efficient exchange of
aerosol particles at cloud-bottom was confirmed by the similarity of the size distribution of BC residuals and BC particles
sampled below-cloud. Last, the increase of BC residuals number concentration (+31%) and geometric mean diameter (+38%)
from the cloud top to the cloud bottom and the absolute enrichment of larger BC residuals compared to outside-cloud supported
30 the hypothesis of concomitant scavenging mechanisms but also suggested the formation of BC agglomerates caused by cloud-

processing. The vertical evolution of BC properties from inside-cloud and below-cloud indicated an efficient aerosol exchange at cloud-bottom, which might include activation, cloud processing, and sub-cloud release of processed BC agglomerates. In the case of persistent low-level Arctic clouds, this cycle may reiterate multiple times, adding one additional degree of complexity to the understanding of cloud processing of black carbon particles in the Arctic.

35 1 Introduction

It is well known that clouds strongly affect the surface energy budget in the Arctic (Shupe and Intrieri, 2004; Lubin and Vogelmann, 2006). However, the interaction between aerosol particles and clouds remains one of the major sources of uncertainty in radiative forcing estimations in the Arctic and on a global scale (Bellouin et al., 2020; IPCC et al., 2021).

Black carbon (BC) particles are carbonaceous aerosol particles emitted by the incomplete combustion of fossil fuels and biomasses (Bond et al., 2004) and, due to their unique absorption of solar radiation in the visible spectrum, they play an important role in the Arctic radiative balance. First, BC particles directly interact with the solar radiation, causing a net warming of the local atmospheric layer (Flanner, 2013). Second, the change in local temperature might influence the vertical distribution of clouds via semi-direct effects (Sand et al., 2013). Third, via aerosol-cloud interaction, also known as the first indirect effect, BC activation might lead to a change in the microphysical properties of clouds, with consequences on cloud radiative properties (Sand et al., 2013). Lastly, after deposition, BC can decrease the snow albedo, promoting melting via the snow darkening effect (Flanner et al., 2009). All of these processes are strongly interconnected (Quinn et al., 2015), making BC the third atmospheric Arctic warmer only after the trace gases carbon dioxide and methane (Oshima et al., 2020).

The seasonality of BC concentration at the Arctic surface is characterized by a maximum in early spring and a minimum in summer (Quinn et al., 2015). A similar seasonality was recently reported on the vertical scale (Jurányi et al., 2023). Given the rarity of BC sources within the Arctic, most of the BC mass reaches the Arctic via long-range transport (Xu et al., 2017). Hence, the seasonal cycle is primarily controlled by the circulation of air masses between the Arctic and southern latitudes (Bozem et al., 2019) and by precipitation events during long-range transport (Croft et al., 2016). Therefore, the ability to understand how BC interacts with clouds (cloud scavenging) is crucial for quantifying the BC burden and radiative forcing in the Arctic region. Overall, cloud scavenging is responsible for 90% of BC mass deposition in the Arctic (Dou and Xiao, 2016), with the highest precipitation rate in summer contributing to the decline in the BC burden from late spring to autumn (Garrett et al., 2011; Mori et al., 2020). Moreover, cloud scavenging influences the vertical distribution of BC in the atmosphere, with convective precipitation controlling the concentration of BC in the upper troposphere, and stratiform precipitation controlling the concentration of BC at the surface (Mahmood et al., 2016). However, the complexity of in-cloud and below-cloud scavenging of BC limits the ability of global models to reproduce the temporal, vertical, and horizontal distribution of BC in the entire Arctic region (Whaley et al., 2022) and, consequently, the radiative forcing of BC (Samset et al., 2013, 2018).

The ability of BC particles to promote droplet formation (hygroscopicity) is one of the most complex parametrisations in global model schemes (Holopainen et al., 2020). In fact, the cloud nucleation ability of BC depends on fundamental particle properties

such as diameter and mixing state, which evolve during atmospheric aging due to condensation and coagulation processes. While fresh BC particles are not hygroscopic, aged BC particles show an increase in hygroscopicity (Schwarz et al., 2015; Ohata et al., 2016) correlated with the particle diameter (Motos et al., 2019a) and the formation of inorganic and organic coatings (Dalirian et al., 2018; Motos et al., 2019b). If considerable progresses have been made on the quantification of BC hygroscopicity, its ability to act as an ice nucleating particle is more uncertain. Despite the lack of measurements, field and laboratory studies classify BC as a non-efficient ice nucleating particle, at least at warm temperatures (Kupiszewski et al., 2016; Kanji et al., 2020).

Arctic relevant processes add an extra level of complexity to the study of cloud scavenging of aerosol and BC particles in liquid and mixed-phase clouds. The nucleation scavenging of aerosol particles from the below-cloud layer represents the dominant activation mechanism in the Alaskan Arctic (Earle et al., 2011; McFarquhar et al., 2011). In contrast, Igel et al. (2017) showed that free-tropospheric aerosol particles may be activated at the top of low-level Arctic clouds protruding into the inversion layer (clouds within inversion; Sedlar et al., 2011), leading to downward transport of free-tropospheric aerosol particles into the boundary layer. Moreover, other in-cloud processes might compete with nucleation scavenging. In fact, interstitial BC particles (BC particles present in the cloud volume but not activated into cloud particles) may be efficiently captured by pre-existing cloud particles via interstitial scavenging (Baumgardner et al., 2008). Despite being often ignored, the number concentration of Arctic aerosol particles is highly sensitive to interstitial scavenging that occurs during long-range transport (Croft et al., 2016). Furthermore, cloud processes such as droplet coalescence, riming, and the Wegener–Bergeron–Findeisen (WBF) modify the size (droplet coalescence and riming) and phase partitioning (riming: from liquid to ice; WBF: from liquid to interstitial) of activated aerosol particles (Ding et al., 2019). In the presence of persistent low-level Arctic clouds, aerosol particles may undergo the cloud processes described above several times. Solomon et al. (2015) identified a recycling mechanism for cloud active aerosol particles that comprises activation at the cloud bottom, growth within the cloud, sedimentation, and release below the cloud layer, followed by reactivation at the cloud bottom. Finally, the understanding of the complex interaction between BC and clouds in the Arctic is further complicated by the rarity of in-situ observations, especially at the cloud level (Tørseth et al., 2019).

In this work, we present unprecedented vertically resolved airborne measurements of BC particles sampled inside and outside clouds in the European Arctic in the summer of 2017 during the Arctic CLOUD Observations Using airborne measurements during polar Day (ACLOUD) campaign (Wendisch et al., 2018, 2022). The objective is to provide the first insights into the BC-cloud interaction in the Arctic with a particular focus on: 1) the presence and properties of cloud-active BC, 2) the scavenging mechanism of BC, and 3) the impact of cloud processing on the vertical distribution of BC.

2 Methodology

The ACLOUD campaign was conducted between 23 May and 26 June 2017 in the northwest region of Svalbard (Norway) within the framework of the “Arctic Amplification: Climate Relevant Atmospheric and Surface Processes, and Feedback

95 Mechanisms (AC)³ project (Wendisch et al., 2018, 2022), see <https://www.ac3-tr.de/>. All validated data are published in the World Data Center PANGAEA as instrument-separated data subsets (Ehrlich et al., 2019b, <https://doi.org/10.1594/PANGAEA.902603>). Flight operations and atmospheric measurements used in the present work are described in the following, while the instrumentation, measured parameters and relative abbreviations are listed in Table 1.

2.1 Flight operations

100 Atmospheric observations were carried out with two research aircrafts of the Alfred Wegener Institute (AWI), the Polar 5 and the Polar 6 (Wesche et al., 2016). The Polar 5 was equipped with remote-sensing instruments, while the Polar 6 was equipped with in-situ measurements. A full list of the deployed instrumentation can be found in Ehrlich et al. (2019). The present study contains the results of three distinct subsets of the ACLOUD flights. The first subset included 12 flights providing vertical measurements of aerosol and cloud particles up to an altitude of 3500 m asl. The flights were performed on 27 May 2017 and
105 on 02, 04, 05, 08, 13, 14, 16, 17, 18, 23, 26 June 2017 over open water, marginal sea ice zone, and ground (Figure 1a). The second subset was composed of 4 flights performed on 02, 04, 05, 08 June 2017 with repeated sampling of low-level clouds over the marginal sea ice zone (Figure 1b), thus providing the best opportunity to investigate the interaction of BC with mixed-phase clouds in the boundary layer. The last subset was composed of one single flight performed on 25 June 2017, representing the sole case of clear-sky conditions (Figure 1b).

110 2.2 Techniques

2.2.1 Meteorological measurements

Meteorological parameters such as pressure (P), relative humidity (RH) and temperature (T) were recorded at 1 Hz resolution with the basic meteorological sensor suite of Polar 6 fully described in previous works (Herber et al., 2012; Schulz et al., 2019; Ehrlich et al., 2019). T and RH data were merged with aircraft position and air pressure into a 1 Hz basic meteorological dataset
115 (<https://doi.org/10.1594/PANGAEA.902849>; Hartmann et al., 2019). The potential temperature (T_p) was calculated from measured ambient temperature (T) and pressure (P) as: $T_p = T (P_0/P)^{0.286}$.

2.2.2 Cloud particle measurements

The Small Ice Detector Mark 3 (SID-3; Hirst et al., 2001; Vochezer et al., 2016) was operated on board the Polar 6 to measure the cloud particle number size distribution in the 5 - 45 μm diameter range (<https://doi.org/10.1594/PANGAEA.900261>;
120 Schnaiter and Järvinen, 2019b). Liquid droplets and ice crystals were distinguished based on the two-dimensional (2-D) scattering patterns for the particle sphericity as described in Vochezer et al. (2016). More details on the data processing of the SID-3, including the correction of coincidence artefacts, can be found in Järvinen et al. (2023). Based on the phase discrimination, we calculated the number concentration of liquid droplets (N_{Dro}), from which the liquid water content (LWC) was estimated assuming spherical particles and a particle density of 1 g cm^{-3} .

125 The Cloud Imaging Probe (CIP, DMT, Longmont, CO, USA; Baumgardner et al., 2001) allows quantifying the dimension and
shape of cloud particles and was used to derive the number concentration of non-spherical ice crystals (N_{ice} ; calculated
according to circularity as in Crosier et al. (2011)) and the ice water content (IWC; calculated with the mass-diameter
relationship defined by Brown and Francis 1995)). The number size distribution of ice crystals presented in this work is based
130 on effective equivalent diameter, which is more comparable with previous Arctic measurements (Mioche et al., 2017). Due to
the significant uncertainties in the probe's sensitive area for the smallest particle sizes, the nominal detection size range was
reduced, in the present work, to 75 - 1550 μm . The mass fraction of ice water (IWF) was calculated from the IWC estimated
by the CIP, and the LWC estimated by the SID-3. The properties of the ice crystals derived from CIP measurements performed
on board the Polar 6 are published in the PANGAEA database (<https://doi.org/10.1594/PANGAEA.899074>; Dupuy et al.,
2019).

135 The Airborne Mobile Aerosol Lidar (AMALi) system was installed on board the Polar 5, and was used to derive the cloud top
height. Previous works provide technical details on the operation principle (Stachlewska, 2005), data processing (Stachlewska
et al., 2010) and Arctic deployment (Nakoudi et al., 2020). Cloud top height with a 10 seconds time resolution are available
on PANGAEA database (<https://doi.org/10.1594/PANGAEA.899962>; Neuber et al., 2019). We will solely discuss the cloud
top height data acquired during collocated flights of Polar 5 with Polar 6 occurred on 27-29 June 2017 and 02-05-08-13-17
140 June 2017.

2.2.3 Aerosol particle measurements

All aerosol particle data presented in this work were acquired with online single-particle instruments on board the Polar 6. A
Single-Particle Soot Photometer (SP2, version D with 8-channels) by Droplet Measurement Technologies (DMT, Longmont,
CO, USA) was used to detect BC aerosol particles. While the operating principles of the SP2 and assumptions used in this
145 study are described briefly in the following, a comprehensive description of calibration standards and procedure is given by
Schwarz et al. (2006), Moteki and Kondo (2010), Gysel et al. (2011) and Laborde et al. (2012). By laser-induced
incandescence, the SP2 is capable of quantifying the mass of absorbing and refractory material contained in aerosol particles
passing through the high-intensity continuous-wave, intra-cavity laser beam at a wavelength of 1064 nm (Stephens et al.,
2003). The incandescence light detector was calibrated with a fullerene soot standard from Alfa Aesar (stock no. 40971, lot
150 no. FS12S011), size selected with a differential mobility analyser (DMA; TSI, Shoreview, MN, USA). The term refractory
black carbon (rBC) is used to identify the insoluble carbonaceous matter that vaporizes at temperatures around 4000 K, and
that is measured with a laser-induced incandescence technique, including the SP2 (Petzold et al., 2013). To facilitate the
reading, the term BC is used instead of rBC to identify all measurements performed with the SP2 and presented hereafter. The
SP2 installed on the Polar 6 provided the number concentration (N_{BC}), mass concentration (M_{BC}) and size distribution of BC
155 particles in the 0.37 - 178 fg mass range, converted to a mass-equivalent diameter (D_{BC}) range of 73 - 575 nm using a fixed
bulk density (void-free) of 1800 kg m^{-3} (Moteki et al., 2010). The BC particles associated with a saturated incandescence signal
were included in the last diameter bin of the size distribution and attributed with the maximum quantifiable mass-equivalent

diameter (575 nm) and mass (178 fg). The geometric mean diameter and modal diameter of the mass size distribution will be abbreviated as D_{BC-Geo} and D_{BC-Mod} , respectively.

160 To estimate the BC mass concentration outside the SP2's detection range, the BC mass size distribution measured by the SP2
may be fitted with a lognormal fit (e.g. Laborde et al., 2013; Zanatta et al., 2018). This correction was not applied to the
ACLOUD data since a clear peak in the number size distribution was rarely resolved, and the mass size distribution often
culminated at the SP2's upper quantification limit. Previous studies showed that the SP2 is sensitive to metal-containing
particles such as hematite and magnetite (Schwarz et al., 2006; Yoshida et al., 2016). Hence, metal-containing dust particles
165 may be misinterpreted as BC, causing a potential overestimation of BC concentration. Compared to BC, hematite and
magnetite are characterized by a lower boiling point and colour-ratio (the ratio of thermal emission in the blue and red
spectrum) but also by slower heating rate in the laser beam of the SP2. Hence, the temporal evolution of incandescence signal
in the laser beam of the SP2 and the colour-ratio were used to identify non-BC metal-containing dust particles. During
ACLOUD, particles associated with a slow rise-time of the incandescence signal were removed, while the colour ratio analysis
170 did not show any clear evidence of the presence of non-BC yet incandescing particles. The optical diameter of BC-free particles
was inferred with Mie theory (Bohren and Huffman, 1998) from the scattering signal acquired by avalanche photodetectors in
the given solid angles under the assumption of spherical particles and a refractive index of $1.50+0i$. The measurement of the
particle scattering cross-section was calibrated using monodisperse spherical polystyrene latex (Thermo Scientific). The
leading-edge only technique was applied to estimate the coating thickness of BC-containing particles from the optical diameter
175 of unperturbed BC cores and BC-containing particles (Gao et al., 2007). The refractive index of the coating was assumed to
be equal to BC-free particles ($1.50 + 0i$), while the refractive index of BC cores was set to be $1.90+0.8i$. The latter, although
being lower than previous Arctic studies ($2.26 + 1.26i$; Raatikainen et al., 2015; Kodros et al., 2018; Zanatta et al., 2018) and
higher than measurements in continental Europe ($1.75 + 0.43i$; Yuan et al., 2021), allowed to match the mass-equivalent
diameter of BC with its optical diameter. The coating thickness was quantified for BC-containing particles having a D_{BC}
180 between 200 nm and 250 nm. It must be noted that the scattering detector failed on 03 June 2017; hence no LEO-fit analysis
was performed on the following flights. BC data acquired with the SP2 are publicly available at
<https://doi.pangaea.de/10.1594/PANGAEA.899937> (Zanatta and Herber, 2019b).

The Ultra High Sensitivity Aerosol Spectrometer (UHSAS; DMT, Longmont, CO, USA) measures the number concentration
(N_{AP}) and size distribution of aerosol particles in the optical diameters range of 60-1000 nm (Cai et al., 2008). The UHSAS
185 was connected in parallel to the SP2 at a tubing length distance of 15 cm. Due to the low signal-to-noise ratio at small sizes,
the concentration and size distribution estimated from the UHSAS during ACLOUD were valid within the optical diameter
range of 80-1000 nm (Zanatta et al., 2020). It must be noted that rapid changes of pressure might affect the sample flow
measurement and, consequently, the quantification of aerosol particle number concentration by the UHSAS (Brock et al.,
2011). Although modification of the UHSAS flow system are recommended for airborne operation (Kupc et al., 2018), Schulz
190 et al. (2019) showed no measuring bias of unmodified UHSAS during low-speed flights installed in the unpressurized cabin

of the Polar 6. Aerosol particles data acquired with the UHSAS are publicly available at <https://doi.pangaea.de/10.1594/PANGAEA.900341> (Zanatta and Herber, 2019a).

2.3 Cloud and aerosol particles sampling

195 Two different inlets were installed on the front top of the aircraft Polar 6, ahead of the engines to sample the total aerosol and cloud particle residuals. A comprehensive description of the two inlets is given by Ehrlich et al. (2019).

The total aerosol inlet was a stainless-steel inlet with a shrouded diffuser already installed on the Polar 6 in previous Arctic campaigns (Leaitch et al., 2016; Schulz et al., 2019). The manifold exhaust flowed freely into the back of the cabin, such that the intake flow varied with the true airspeed of the aircraft. Sampling speed at the inlet tip was approximately isokinetic for the airspeeds during ACLOUD, leading to a near-unity transmission of submicrometric aerosol particles (Ehrlich et al., 2019).

200 A counterflow virtual impactor (CVI; Ogren et al., 1985; Noone et al., 1988) allowed size selective sampling of cloud particles by use of a counterflow at the inlet tip. Depending on the velocity of the particles inside the inlet and the flow rate of the counterflow, smaller cloud and aerosol particles may be decelerated, stopped, and blown out of the inlet. Due to the rather low velocity of the Polar 6, only cloud particles larger 10 μm could be sampled inside clouds by the CVI, while interstitial aerosol and gases and smaller droplets were pre-segregated. Cloud residual particles were then released following evaporation or
205 sublimation of liquid droplets or ice crystals, respectively. Hence, cloud particle residuals were representative of cloud condensation nuclei and/or ice nucleating particles (Mertes et al., 2005, 2007). In order to calculate the concentration of cloud particle residuals, the enrichment factor (EF) needed to be considered. EF was calculated as the ratio between the air volume flows in front and within the CVI, which varied between a minimum of 3.2 and maximum of 5.4 with a median value of 4.2. The transmission efficiency (TE) within the CVI inlet was calculated, similar to Schroder et al. (2015), as the ratio of the
210 number concentration of droplets larger than the CVI size cut-off (10 μm ; $N_{\text{Dro-10}}$) measured by the SID-3 over the number concentration of aerosol particles measured by the UHSAS in the optical diameter range of 80-1000 nm and corrected by the enrichment factor of the CVI inlet. Overall, TE varied between a flight average minimum of 16% (05 June) to a maximum of 23% (on 08 June), with an overall median value of 21%. Finally, the number concentration of BC in cloud particle residuals ($N_{\text{BC-res}}$) was calculated as:

$$N_{\text{BC-res}} = \frac{N_{\text{BC}}}{\text{EF} \times \text{TE}} \quad 1$$

215

The SP2 and the UHSAS were operated in parallel and shared a sampling line which was alternatively connected to the total inlet or the CVI inlet. Outside clouds ($N_{\text{Dro}} = 0 \text{ cm}^{-3}$ and $\text{LWC} = 0 \text{ g m}^{-3}$), SP2 and UHSAS measurements were performed at the total inlet. Inside cloud ($N_{\text{Dro}} \geq 1 \text{ cm}^{-3}$ and $\text{LWC} \geq 0.01 \text{ g m}^{-3}$), the SP2 and UHSAS were sampling throughout the CVI inlet line.

3.1 Overview of vertical distribution of BC particles during ACLOUD

Twelve ACLOUD flights were selected to investigate the vertical profile of BC and cloud particles over the marginal sea ice zone, open water and land in the northwest of Svalbard (Figure 1a). These measurements covered the three synoptic conditions identified during the ACLOUD campaign (Knudsen et al., 2018). One flight (27 May 2017) was performed during the “cold period” when cold and dry conditions were dominant, four flights (02, 04, 05, 08 June 2017) were performed during the “warm period” in the presence of moist air, and seven flights (13, 14, 16, 17, 18, 23, 26 June 2017) were affected by a mixture of air masses, “normal period”.

The vertical variability of M_{BC} and mass size distribution is shown in Figure 2a and Figure 2b, respectively. For this specific analysis, the in-cloud measurement periods were excluded. Overall, the median M_{BC} was 2.3 ng m^{-3} with an interquartile range of $0.86\text{--}4.8 \text{ ng m}^{-3}$. This low concentration is expected during summer across the full Arctic (Schwarz et al., 2013; Roiger et al., 2015; Schulz et al., 2019) and is connected with limited south-north circulation of airmasses (Bozem et al., 2019) and efficient wet removal south of the polar dome (Croft et al., 2016). Although the impact of pollution plumes is not infrequent in the free troposphere in the summer Arctic (Roiger et al., 2015), the average vertical profile of M_{BC} did not show any relevant pollution plume above 500 m asl, where the M_{BC} median concentration varied between 1.7 ng m^{-3} and 3.9 ng m^{-3} . On the contrary, M_{BC} showed a marked decrease to less than 1 ng m^{-3} at altitudes below 500 m asl. Similar to the mass concentration, the mass size distribution remained relatively stable above 500 m (geometric mean of the mass size distribution between 180 nm and 190) but showed an increasing concentration of larger BC particles in the lowermost atmospheric layers, where the geometric mean of the mass size distribution was 220 - 250 nm. While the diameter of BC particles was reported to slightly decrease with altitude in summer in various Arctic regions (Jurányi et al., 2023), the presence of large BC particles in the lowest atmospheric layer is unusual for summer conditions (Arctic Ocean; Taketani et al., 2016). These larger particles (mass geometric mean diameter above 400 nm) accounted for less than 5% of the total number concentration along the full altitude range. Nonetheless, they represented 37% of the total BC mass observed in the lowest 500 m asl, and 17% in atmospheric layers aloft. No evident change in mass concentration and size distribution was observed between the cold, warm and normal periods.

During ACLOUD, cloud cover exceeded 70%, with a preponderant occurrence of low-level clouds (Wendisch et al., 2018). AMALI lidar measurements, performed on board the Polar 5 during collocated flights, confirmed the presence of low-level clouds. The resulting vertical distribution of cloud top height frequency (Figure 2c) showed that 40% of the total clouds were observed below 500 m asl. Due to the variation of BC properties in concurrence with the cloud presence in the lowest 500 m of altitude, in the following, we investigate the relationship between BC properties and low-level clouds to understand the interaction of BC particles with clouds in the summer Arctic boundary layer.

3.2 Identification and characterization of low-level clouds

Within the “warm period” of the ACLOUD campaign, four consecutive flights (02, 04, 05, 08 June 2017), conducted northwest of Svalbard between approximately 80°N and 82°N (Figure 1b), allowed investigating the variability of BC particles above-cloud and below-cloud, and the properties of BC residuals inside clouds. A full description of the atmospheric structure, vertical variability of the water content, and vertical coverage of aerosol particle measurements is given in the supplementary material and shown in Figure S1. The vertical profile of the potential temperature (Figure S1a) indicated that clouds were coupled with the surface (Gierens et al., 2020) and protruded into the inversion layer but not above the inversion top, hence classified as “cloud inside inversion” (Sedlar et al., 2011). In the relatively warm and moist boundary layer ($T > -6.5^{\circ}\text{C}$ and $\text{RH} > 80\%$; Figure S1b), liquid droplets dominated the cloud water content (Figure S1c), while the ice phase was observed throughout the cloud and precipitation was detected below the cloud (Figure S1d). The cloud events discussed here showed many features common to Arctic persistent mixed-phase clouds as summarized by Sedlar et al. (2011), Morrison et al. (2012) and Korolev et al. (2017): dominance of supercooled droplets, intruding-inversion clouds but coupled with the surface, and ice sedimentation below-cloud. We can thus conclude that the selected ACLOUD cloud cases fairly represented summer Arctic conditions. Valid cloud residual measurements were performed from 60 m to 544 m asl (cloud thickness of 310 - 435 m). Above-cloud observations performed above inversion top (400 - 750 m asl) represented free-tropospheric conditions, while below-cloud observations (60 - 150 m asl) represented the Arctic boundary layer influenced by cloud presence (Figure S1e). The measurement time above, inside and below clouds was of 82, 199 and 84 minutes, respectively. Dominant clear sky conditions were observed on 25 June 2017 (ACLOUD normal period) over sea ice north of Svalbard (Figure 1b), where neither cloud droplets nor ice crystals were observed above and below inversion.

3.3 BC properties in a cloud-dominated boundary layer

To understand if cloud presence might affect the properties of BC particles in the boundary layer, we will present the variability of concentration and size distribution of BC particles from above-cloud to below-cloud for the cloud events observed between 02 and 08 June 2017, and from above inversion to below inversion for the clear sky event on 25 June 2017.

The flight ensemble median BC mass concentration decreased by a factor of 4 from above-cloud (median $M_{\text{BC}}=5.5 \text{ ng m}^{-3}$) to below-cloud (median $M_{\text{BC}}=1.3 \text{ ng m}^{-3}$) for the flights occurred between 02 and 08 June, in agreement with the overall vertical profile shown Figure 2a.

For all the considered events, the mass size distribution of BC above-cloud remained almost constant, with an overall geometric mean diameter ($D_{\text{BC-Geo}}$) of 192 nm and a modal diameter ($D_{\text{BC-Mod}}$) of 178 nm. Similar values were observed in the free troposphere under clear-sky conditions on 25 June ($D_{\text{BC-Mod}} = 183 \text{ nm}$, $D_{\text{BC-Geo}} = 190 \text{ nm}$; Figure 3d). The steady state of BC size distribution from 02 June to 25 June indicated the presence of a homogeneous BC population in the free troposphere, which appeared to be independent of cloud presence below inversion-top. The mass size distribution of BC aerosol below-cloud, characterized by a $D_{\text{BC-Mod}}$ of 193 nm and a $D_{\text{BC-Geo}}$ of 255 nm, was enriched in larger BC particles otherwise not

observed in the free troposphere (Figure 3b). In fact, BC particles larger than the saturation-diameter (575 nm) represented less than 5% of M_{BC} above-cloud and 36% of M_{BC} below-cloud. In contrast, the BC mass size distribution observed in clear-sky conditions (25 June) within the boundary was depleted in particles larger than 150 - 200 nm and did not show any mode in the SP2 size detection range (Figure 3d). The size distribution of free-tropospheric BC observed during ACLOUD is not uncommon in the Arctic spring and summer (Raatikainen et al., 2015; Taketani et al., 2016; Kodros et al., 2018; Zanatta et al., 2018; Schulz et al., 2019; Ohata et al., 2021). However, none of these previous Arctic studies reported BC size distributions similar to below-cloud conditions. The results presented in this section confirmed the vertical variability of BC concentration and size presented in Section 3.1, clearly showing that ground observations did not represent the free troposphere. Moreover, the recurring enhancement of larger BC particles observed below-cloud compared to above-cloud and its depletion in a clear-sky boundary layer suggested the influence of cloud processing on BC properties.

3.4 BC scavenging processes

The number concentration of BC residuals was little, with a median N_{BC-res} of 0.58 cm^{-3} and an interquartile range of 0.29 - 1.0 cm^{-3} . The N_{BC-res}/N_{Dro10} ratio ranged from a maximum median of 1.5% on 02 June to a minimum median of 0.69% on 04 June, with a cloud ensemble median of 0.90% and an interquartile range of 0.46 - 1.4% (Figure 4a). The low N_{BC-res}/N_{Dro10} values indicated that BC was activated in a small fraction of droplets and represented the minority of cloud-active aerosol particles. Considering that the number size distribution culminated at the low quantification limit of the SP2, N_{BC-res} and N_{BC-res}/N_{Dro10} were, most certainly, underestimated. To assess the activation mechanism of BC particles, we compared the absolute and relative concentration of BC residuals with BC particles sampled outside clouds.

3.4.1 Below-cloud nucleation scavenging

Earle et al. (2011) and McFarquhar et al. (2011) found that the totality of below-cloud aerosol particles was activated in-cloud in the Alaskan Arctic. Following their approach, we calculated the ratio between N_{BC-res} over N_{BC} measured below-cloud (N_{BC-blw}) and above-cloud (N_{BC-abv}). N_{BC-res}/N_{BC-abv} varied from the highest median value of 0.44 on 02 June to the lowest median value of 0.25 on 08 June, with a cloud ensemble median of 0.30 (IQR=0.18-0.47; Figure 4b). The N_{BC-res}/N_{BC-blw} median values were surprisingly high, ranging from a minimum of 1.05 on 02 June and a maximum of 1.33 on 04 June, with a cloud ensemble median of 1.16 and an interquartile range of 0.71-1.76 (Figure 4c). The above unity values of N_{BC-res}/N_{BC-blw} suggested that the totality of BC particles below-cloud could be activated in cloud via adiabatic lifting (Earle et al., 2011; McFarquhar et al., 2011). However, measurement uncertainty might contribute to the N_{BC-res}/N_{BC-blw} values above unity. The uncertainty of N_{BC-res} had two main contributions: the 1σ reproducibility of N_{BC} measured by SP2 (5%; Laborde et al., 2012), and the uncertainty associated with the transmission efficiency factor (13%). The latter was estimated by propagating the 1σ reproducibility associated with N_{AP} measured by the UHSAS (9%; Ehrlich et al., 2019) and the uncertainty of N_{Dro} measured by the SID-3 (10%; Baumgardner et al., 2017). The overall uncertainty of N_{BC-res}/N_{BC-blw} ($\pm 15\%$) might thus contribute to the N_{BC-res}/N_{BC-blw}

up to 1.15. Moreover, the sedimentation of ice crystals observed below-cloud (Figure S1d) might reduce $N_{\text{BC-blw}}$ by impaction
315 scavenging (Hegg et al., 2011; Gogoi et al., 2018), hence contributing to the enhanced $N_{\text{BC-res}}/N_{\text{BC-blw}}$ values.

3.4.2 Interstitial and cloud top scavenging

Other activation mechanisms might contribute to the $N_{\text{BC-res}}/N_{\text{BC-blw}}$ values above unity. First, interstitial aerosol particles may
be scavenged via impaction with existing droplets (Croft et al., 2016), increasing the number concentration of BC residuals
(Baumgardner et al., 2008). We thus compared the fraction of BC particles measured outside clouds ($F_{\text{BC}} = N_{\text{BC}}/N_{\text{AP}}$) and inside
320 clouds ($F_{\text{BC-res}} = N_{\text{BC-res}}/N_{\text{AP-res}}$). An increase in $F_{\text{BC-res}}$ compared to F_{BC} , indicate interstitial impaction as the preponderant
scavenging mechanism of BC particles (Baumgardner et al., 2008). During the ACLOUD cases, we found slightly smaller
 $F_{\text{BC-res}}$ (1.0%) than F_{BC} above-cloud (2.3%) and below-cloud (1.2%). Similar $F_{\text{BC-res}}$ and F_{BC} below-cloud suggested that BC
was activated via the same pathway of the bulk aerosol, that BC and other aerosol particles shared similar hygroscopicity, and
that BC particles were not entering, preferentially, the cloud phase by interstitial scavenging. Second, Igel et al. (2017) showed
325 that free-tropospheric aerosol may be scavenged at the top of stratocumulus Arctic clouds protruding through the inversion
layer. Considering that the clouds observed between 02 and 08 June extended into the inversion layer (Figure S1a and Figure
6a), the high N_{BC} observed above-cloud represented a non-negligible source of hygroscopic BC particles which might have
contributed to $N_{\text{BC-res}}/N_{\text{BC-blw}}$ values above unity reported above. To better understand the contribution of below-cloud and
above-cloud activation processes, we further analysed the size distribution and mixing state of BC residuals in Section 3.5 and
330 its vertical variability in Section 3.6.

3.5 Characterization of BC residual properties

Diameter and mixing state are fundamental properties controlling the ability of aerosol particles to nucleate a liquid droplet
(hygroscopicity). Previous studies showed that larger and internally mixed BC are more hygroscopic (Dalirian et al., 2018;
Motos et al., 2019a) and are enriched in the residual phase compared to outside clouds (Motos et al., 2019b). Hence, to assess
335 the nucleation scavenging during ACLOUD, we present the coating thickness and size distribution of BC residuals and their
variation compared to outside cloud conditions. Due to failure of the scattering detector, the quantification of coating thickness
was only possible for the flight occurred on 02 June. Considering that the coating thickness was quantified for BC cores in the
200 - 250 nm diameter range, which represented a small subset of the total detected BC particles, the results discussed below
are extremely uncertain due to the low counting statistics.

340 3.5.1 Coating thickness of BC residuals on 02 June

First, it should be noted that the coating thickness analysis was applied only to BC particles in the 200-250 nm range of mass-
equivalent diameter. BC particles in this diameter range were ubiquitously found above-cloud, inside-cloud and below-cloud
(Figure 3). The distribution of coating thickness is presented in Figure S2 in the supplementary material. The thinnest coatings
were observed above clouds, where the coating thickness median was 30 nm (IQR = 23 - 48 nm) and the median shell-to-core

345 ratio was 1.51 (IQR = 1.38 - 1.8). The thickest coatings were observed below clouds, where the median coating thickness was 43 nm (IQR = 25 - 58 nm), and the median shell-to-core diameter ratio was 1.67 (IQR = 1.43 - 1.98). The BC cloud residuals showed medium coating thickness (median = 38 nm, IQR = 25 - 59 nm) and shell-to-core ratio (median = 1.58, IQR = 1.39 - 1.92 nm) compared to above-cloud and coatings to below-cloud. The coating thickness values presented here are similar to previous Arctic ground (Raatikainen et al., 2015; Zanatta et al., 2018) and airborne (Kodros et al., 2018; Ohata et al., 2021) observations and are substantially higher than urban observations (Laborde et al., 2013; Yoshida et al., 2020). Even though thicker coatings can be found in aged continental air masses, the presence of 30-40 nm thick coatings is sufficient to significantly increase the hygroscopicity of otherwise hydrophobic uncoated BC particles in laboratory experiments (Dalirian et al., 2018) and field observations (Motos et al., 2019a). Keeping in mind the low counting statistics of the coating analysis, we can conclude that BC particles sampled during ACLOUD represented aged and hygroscopic BC particles, which could be efficiently activated via nucleation scavenging. However, the reduced temporal coverage and the uncertainty of coating thickness quantification (17%; Laborde et al., 2012) did not allow identifying a significant change in the degree of internal mixing between BC residuals and BC particles sampled outside clouds.

3.5.2 Size distribution of BC residuals

The mass size distribution of BC residuals was similar during all cloud cases (Figure 3c), indicating similar conditions along the measuring period. While an evident mode at 193 nm was comparable to BC particles observed above and below cloud, the size distribution of BC residuals showed a prominent shoulder towards larger diameters, culminating in the overflow saturation bin (BC cores larger than 575 nm of mass-equivalent diameter, representing 28% of the M_{BC-res}). This feature was shared only with BC particles sampled below-cloud. The almost bimodal distribution observed inside-cloud and below-cloud suggested the occurrence of different cloud processes. On one side, the recurring peak around 180-200 nm in the BC size distribution outside and inside cloud reinforced the hypothesis of cloud-mediated transport of free-tropospheric BC in the boundary layer proposed by (Igel et al. (2017)). On the other side, the similar size distributions of BC residuals and BC particles sampled below-cloud clearly indicated an efficient exchange of BC particles at the cloud bottom. This exchange might include nucleation from the below-cloud layer (Earle et al., 2011; McFarquhar et al., 2011) followed by the release of BC residuals contained in precipitating droplets below-cloud (Igel et al., 2017). As suggested for ice nucleating particles in persistent low-level Arctic clouds by Solomon et al. (2015), this activation and release cycle might occur several times.

To quantify the size-dependent enrichment or depletion of BC in cloud residuals compared to outside cloud, we calculated the ratio of the number size distribution of BC residuals over the number size distribution of BC particles sampled above-cloud and below-cloud. BC residuals were depleted compared to above-cloud BC particles, especially in the 80-300 nm D_{BC} range (Figure 5a). However, BC particles larger than 400 nm were exponentially enriched in cloud residuals by a 1.5-3.5 factor compared to above-cloud conditions. The ratio of the number size distribution was different for below-cloud BC (Figure 5b), where it increased from approximately 1 for D_{BC} below 100 nm to values around 1.5 for D_{BC} larger than 200 nm. First, these results confirmed that larger and more hygroscopic BC particles are usually enriched in cloud residuals (Motos et al., 2019a).

Second, the values above unity shown in Figure 5, indicating an absolute enrichment of larger BC residuals compared to above-cloud and below-cloud, suggested the formation of these larger BC as the result of in-cloud processing.

380 3.6 Vertical structure of cloud microphysics and BC residuals

In the following, we investigate the vertical variability of the cloud phase and BC residuals to understand the influence of activation from above-cloud and below-cloud and to identify any potential cloud processes and their potential effects on BC residuals properties.

3.6.1 Normalized altitudes

385 Due to the low counting statistics caused by the low concentration of ice crystals and BC particles, this analysis is based exclusively on the cloud ensemble. Since cloud top and cloud bottom height showed some variability during the different flights (Figure S1), the vertical variability of cloud and residual properties are presented as a function of the in-cloud normalized altitude (Z_n) following Mioche et al. (2017) as:

$$Z_n = \frac{Z - Z_b}{Z_t - Z_b} \quad 2$$

Where Z is the measurement altitude, Z_b is the lowest altitude of in-cloud valid BC residual measurements and Z_t is highest altitude of in-cloud BC residual measurements. Thus, $Z_n = 1$ and $Z_n = 0$ correspond to the highest and lowest BC residuals measurement, respectively. Considering the relatively thin clouds (vertical extent between 310 - 435 m), the cloud layer was divided into 4 vertical sections (quartiles).

3.6.2 In-cloud vertical profiles

The vertical profile of potential temperature indicated the presence of a homogenous and well-mixed cloud section extending from cloud bottom to $Z_n = 0.75$, where median T_{Pot} values varied within 0.25 K. Increasing T_{Pot} at $Z_n > 0.75$ indicated the cloud intrusion in the inversion layer (Figure 6a). The LWC showed an increasing trend from cloud bottom until $Z_n = 0.75$ where the median LWC was 0.27 g m^{-3} and a decreasing trend in the upper quartile of the cloud ensemble (Figure 6b). The IWC increased by two orders of magnitude from $1.4 \times 10^{-4} \text{ g m}^{-3}$ at cloud top to $1.8 \times 10^{-2} \text{ g m}^{-3}$ at cloud bottom (Figure 6c). The number concentration of BC residuals increased monotonically from 0.50 cm^{-3} at cloud top to 0.73 cm^{-3} at cloud bottom (Figure 6d).
400 The relative change of $N_{\text{BC-res}}$ between vertically-adjacent quartiles was in the uncertainty range (14%, see Section 2.2.3), while the T-test analysis indicated that the hypothesis of equal $N_{\text{BC-res}}$ averages was confirmed for the two lowermost quartiles ($Z_n < 0.50$), but not for the two uppermost quartiles ($Z_n > 0.5$). Thus, we cannot conclude that the vertical trend (quartile-by-quartile) of $N_{\text{BC-res}}$ was statistically significant. However, the cloud top ($Z_n > 0.75$) and the cloud bottom ($Z_n < 0.25$) showed a statistically significant difference, not only in the number concentration of BC residuals but also in potential temperature and cloud phase.
405 We thus directly compare the cloud top to the cloud bottom.

3.6.3 BC residuals properties in a liquid cloud top and in a mixed-phase cloud bottom

In the upper quartile of the cloud, while liquid droplets dominated the cloud phase (IWF \sim 0%), only 0.8% of droplets contained an BC residual, and the mass size distribution of BC residuals showed a dominant peak around 200 nm ($D_{\text{BC-Mod}} = 188$ nm; Figure 7), similar to above-cloud BC (Figure 3a). However, a marked tail towards larger diameters was present in the mass size distribution ($D_{\text{BC-Geo}} = 231$ nm), being more similar to below-cloud conditions (Figure 3b). The BC residuals with a mass-equivalent diameter larger than 400 nm accounted for 36% of the total BC mass at the cloud top, being closer to below-cloud values (45%) than above-cloud (11%) values. The cloud phase and BC residuals properties were different at the cloud bottom. Less and smaller liquid droplets but more and larger ice crystals (Figure S3) lead to an increase in IWF up to 14% at the cloud bottom, where higher $N_{\text{BC-res}}$ was observed (+31%) compared to the cloud top, and 1.3% of liquid droplets contained an BC residual. The mass size distribution of BC residuals at cloud-bottom was almost identical to the cloud top for D_{BC} below 200 nm (Figure 7). However, due to the increasing concentration of larger BC residuals at cloud-bottom, we did not observe a clear peak in the mass size distribution (as observed at the cloud top, above-cloud, and below-cloud) leading to a $D_{\text{BC-Geo}}$ of 318 nm (+38% compared to the cloud top). Overall, BC residuals larger than 400 nm accounted for the majority of the total $M_{\text{BC-res}}$ (62%) at the cloud bottom.

The data presented in this section showed for the first time that the population of BC residuals in an Arctic cloud is not homogeneous on the vertical scale, indicating that BC might be scavenged or processed via different pathways, complicating the interpretation of our results. Considering the activation mechanisms, the higher concentration of BC residuals at the cloud bottom suggests the predominant activation at the cloud bottom (Earle et al., 2011). However, the increase in T_{Pot} at the cloud top confirmed the intrusion of the cloud into the inversion layer (Sedlar et al., 2011) and reinforces the hypothesis of nucleation scavenging of free-tropospheric BC at the cloud top (Igel et al., 2017), which might contribute to higher concentration of $N_{\text{BC-res}}$ compared to $N_{\text{BC-blw}}$ (Figure 4c). If the preferential nucleation scavenging of larger BC particles (Motos et al., 2019a, b) might explain the diameter increase inside the cloud respect to outside the cloud (Figure 5), cloud processing might also contribute to the metamorphism of BC residuals within the cloud. Drizzle droplets, observed during the warm period of ACLOUD (Järvinen et al., 2023), may collect multiple droplets during sedimentation. Hence, a few large drizzle droplets may contain multiple BC residuals, which might be released as larger BC agglomerates after evaporation (Ding et al., 2019). Due to the low transmission efficiency of large drizzle drops in the CVI inlet, we were unable to verify the correlation between the diameter of BC residuals and the concentration of drizzling drops. However, below-cloud release via evaporation (Igel et al., 2017) of BC-agglomerates formerly contained in drizzling drops, and its reactivation at cloud-bottom (Solomon et al., 2015) might contribute to the presence of larger BC residuals at cloud-bottom (Figure 7) and explain the similarity between in-cloud and below-cloud size distribution (Figure 3b,c). The increase in IWC at cloud-bottom adds one additional degree of complexity. As shown by Ding et al. (2019), different processes such WBF and riming might modify the phase partitioning and size distribution of BC residuals in mixed-phase clouds. With our dataset we were, however, unable to confirm nor to exclude the occurrence of liquid and ice driven metamorphism of BC residuals.

4 Conclusion

440 The interaction of BC particles with Arctic clouds was investigated with airborne measurements in the northwest of Svalbard (Norway) in the framework of the ACLOUD campaign in summer 2017. The overall vertical variability of BC properties during the ACLOUD campaign indicated a net decrease of BC mass concentration and an increase in BC diameter in the lowest atmospheric layer dominated by clouds. Four case events characterized by the presence of low-level, surface-coupled, inside-inversion and mixed-phase clouds were identified.

445 The analysis of these events confirmed a net separation of BC properties from the atmospheric layers above-cloud in the free troposphere to the below-cloud layer, where less (median BC mass concentration of 1.4 ng m^{-3}), larger (geometric mean of the mass size distribution of 251 nm) and more coated (median coating thickness of 43 nm) BC particles were observed compared to above-cloud conditions (median BC mass concentration of 5.5 ng m^{-3} , geometric mean of the mass size distribution of 189 nm, and median coating thickness of 30 nm). In the absence of clouds, BC particles in the boundary layer were dominated by
450 small diameters (geometric mean of the mass size distribution of 147 nm).

Under mixed-phase cloud conditions (median temperature of -5.3°C , median LWC of 0.15 g cm^{-3} , and median IWC of 0.002 g cm^{-3}), only a small minority of droplets (less than 1%) contained an BC particle. It appeared that the totality of BC particles below the cloud layer was activated, with potential activation of free-tropospheric BC in the cloud top extending in the inversion layer. The population of cloud residuals was enriched in larger BC particles compared to above-cloud conditions
455 (geometric mean of the mass size distribution of 249 nm) very similar to below-cloud BC. This similarity suggested efficient exchange of BC particles between the cloud and below-cloud layers. The vertical profiling of the cloud layer showed a clear stratification of BC residuals properties from the liquid cloud-top protruding in the inversion layer to the mixed-phase cloud-bottom, potentially suggesting metamorphism of BC residuals caused by cloud processing.

To conclude, the ACLOUD observations demonstrated that surface measurements are clearly not representative of the
460 atmosphere aloft. This statement becomes particularly important in the presence of low-level mixed-phase, persistent clouds, when recurring cloud processing may influence not only the vertical distribution of BC but also its microphysical properties inside-cloud and below-cloud. Considering the short duration of our measurements and the complexity of aerosol-cloud interaction, more observations are needed to constrain activation mechanisms of BC and the impacts of cloud processing in the Arctic.

465

Code and data availability

The SP2 data were analysed with PSI Toolkit single particle soot photometer (SP2), version 4.110. Contact Droplet Measurement Technologies to download the software.

470 *Author contributions*

The manuscript was written by MZ with contributions from all authors. Cloud particle measurements and subsequent data analysis were performed by OJ, RD, EJ and MS. Aerosol particle measurements and subsequent data analysis were performed by MZ AH, ZJ, SM, OE and JS. All authors contributed to the data interpretation.

475 *Acknowledgements*

The authors thank Christof Lüpkes (Alfred-Wegener-Institut, Helmholtz-Zentrum für Polar- und Meeresforschung (AWI), Bremerhaven, Germany) and Roland Neuber (Alfred-Wegener-Institut, Helmholtz-Zentrum für Polar- und Meeresforschung (AWI), Potsdam, Germany) for the valuable technical and scientific discussion.

480 *Financial support*

We gratefully acknowledge the funding by the Deutsche Forschungsgemeinschaft (DFG, German Research Foundation)–project ID 268020496 – TRR 172, within the Transregional Collaborative Research Center “Arctic Amplification: Climate Relevant Atmospheric and Surface Processes, and Feedback Mechanisms (AC)3”. Marco Zanatta acknowledges funding by the Deutsche Forschungsgemeinschaft (DFG, German Research Foundation, grant no. Projektnummer 457895178). Emma
485 Järvinen acknowledges funding through the Helmholtz Association’s Initiative and Networking Fund (grant agreement no. VH-NG-1531).

References

- Baumgardner, D., Jonsson, H., Dawson, W., O'Connor, D., and Newton, R.: The cloud, aerosol and precipitation spectrometer: a new instrument for cloud investigations, *Atmospheric Res.*, 59–60, 251–264, [https://doi.org/10.1016/S0169-8095\(01\)00119-3](https://doi.org/10.1016/S0169-8095(01)00119-3), 2001.
- Baumgardner, D., Subramanian, R., Twohy, C., Stith, J., and Kok, G.: Scavenging of black carbon by ice crystals over the northern Pacific, *Geophys. Res. Lett.*, 35, <https://doi.org/10.1029/2008GL035764>, 2008.
- Baumgardner, D., Abel, S. J., Axisa, D., Cotton, R., Crosier, J., Field, P., Gurganus, C., Heymsfield, A., Korolev, A., Krämer, M., Lawson, P., McFarquhar, G., Ulanowski, Z., and Um, J.: Cloud Ice Properties: In Situ Measurement Challenges, *Meteorol. Monogr.*, 58, 9.1-9.23, <https://doi.org/10.1175/AMSMONOGRAPHS-D-16-0011.1>, 2017.
- Bellouin, N., Quaas, J., Gryspeerdt, E., Kinne, S., Stier, P., Watson-Parris, D., Boucher, O., Carslaw, K. S., Christensen, M., Daniau, A.-L., Dufresne, J.-L., Feingold, G., Fiedler, S., Forster, P., Gettelman, A., Haywood, J. M., Lohmann, U., Malavelle, F., Mauritsen, T., McCoy, D. T., Myhre, G., Mülmenstädt, J., Neubauer, D., Possner, A., Rugenstein, M., Sato, Y., Schulz, M., Schwartz, S. E., Sourdeval, O., Storelvmo, T., Toll, V., Winker, D., and Stevens, B.: Bounding Global Aerosol Radiative Forcing of Climate Change, *Rev. Geophys.*, 58, e2019RG000660, <https://doi.org/10.1029/2019RG000660>, 2020.
- Bohren, C. F. and Huffman, D. R.: *Absorption and Scattering of Light by Small Particles*, Wiley-VCH Verlag GmbH, Weinheim, Germany, 1998.
- Bond, T. C., Streets, D. G., Yarber, K. F., Nelson, S. M., Woo, J.-H., and Klimont, Z.: A technology-based global inventory of black and organic carbon emissions from combustion, *J. Geophys. Res. Atmospheres*, 109, D14203, <https://doi.org/10.1029/2003JD003697>, 2004.
- Bozem, H., Hoor, P., Kunkel, D., Köllner, F., Schneider, J., Herber, A., Schulz, H., Leaitch, W. R., Aliabadi, A. A., Willis, M. D., Burkart, J., and Abbatt, J. P. D.: Characterization of transport regimes and the polar dome during Arctic spring and summer using in situ aircraft measurements, *Atmospheric Chem. Phys.*, 19, 15049–15071, <https://doi.org/10.5194/acp-19-15049-2019>, 2019.
- Brock, C. A., Cozic, J., Bahreini, R., Froyd, K. D., Middlebrook, A. M., McComiskey, A., Brioude, J., Cooper, O. R., Stohl, A., Aikin, K. C., Gouw, J. A. de, Fahey, D. W., Ferrare, R. A., Gao, R.-S., Gore, W., Holloway, J. S., Hübler, G., Jefferson, A., Lack, D. A., Lance, S., Moore, R. H., Murphy, D. M., Nenes, A., Novelli, P. C., Nowak, J. B., Ogren, J. A., Peischl, J., Pierce, R. B., Pilewskie, P., Quinn, P. K., Ryerson, T. B., Schmidt, K. S., Schwarz, J. P., Sodemann, H., Spackman, J. R., Stark, H., Thomson, D. S., Thornberry, T., Veres, P., Watts, L. A., Warneke, C., and Wollny, A. G.: Characteristics, sources, and transport of aerosols measured in spring 2008 during the aerosol, radiation, and cloud processes affecting Arctic Climate (ARCPAC) Project, *Atmospheric Chem. Phys.*, 11, 2423–2453, <https://doi.org/10.5194/acp-11-2423-2011>, 2011.
- Brooks, I. M., Tjernström, M., Persson, P. O. G., Shupe, M. D., Atkinson, R. A., Canut, G., Birch, C. E., Mauritsen, T., Sedlar, J., and Brooks, B. J.: The Turbulent Structure of the Arctic Summer Boundary Layer During The Arctic Summer Cloud-Ocean Study, *J. Geophys. Res. Atmospheres*, 122, 9685–9704, <https://doi.org/10.1002/2017JD027234>, 2017.

- 520 Brown, P. R. A. and Francis, P. N.: Improved Measurements of the Ice Water Content in Cirrus Using a Total-Water Probe, *J. Atmospheric Ocean. Technol.*, 12, 410–414, [https://doi.org/10.1175/1520-0426\(1995\)012<0410:IMOTIW>2.0.CO;2](https://doi.org/10.1175/1520-0426(1995)012<0410:IMOTIW>2.0.CO;2), 1995.
- Cai, Y., Montague, D. C., Mooiweer-Bryan, W., and Deshler, T.: Performance characteristics of the ultra high sensitivity aerosol spectrometer for particles between 55 and 800 nm: Laboratory and field studies, *J Aerosol Sci*, 39, 759–769, <https://doi.org/10.1016/j.jaerosci.2008.04.007>, 2008.
- 525 Croft, B., Martin, R. V., Leaitch, W. R., Tunved, P., Breider, T. J., D’Andrea, S. D., and Pierce, J. R.: Processes controlling the annual cycle of Arctic aerosol number and size distributions, *Atmos Chem Phys*, 16, 3665–3682, <https://doi.org/10.5194/acp-16-3665-2016>, 2016.
- Crosier, J., Bower, K. N., Choulaton, T. W., Westbrook, C. D., Connolly, P. J., Cui, Z. Q., Crawford, I. P., Capes, G. L., Coe, H., Dorsey, J. R., Williams, P. I., Illingworth, A. J., Gallagher, M. W., and Blyth, A. M.: Observations of ice multiplication in
530 a weakly convective cell embedded in supercooled mid-level stratus, *Atmospheric Chem. Phys.*, 11, 257–273, <https://doi.org/10.5194/acp-11-257-2011>, 2011.
- Dalirian, M., Ylisirniö, A., Buchholz, A., Schlesinger, D., Ström, J., Virtanen, A., and Riipinen, I.: Cloud droplet activation of black carbon particles coated with organic compounds of varying solubility, *Atmospheric Chem. Phys.*, 18, 12477–12489, <https://doi.org/10.5194/acp-18-12477-2018>, 2018.
- 535 Ding, S., Zhao, D., He, C., Huang, M., He, H., Tian, P., Liu, Q., Bi, K., Yu, C., Pitt, J., Chen, Y., Ma, X., Chen, Y., Jia, X., Kong, S., Wu, J., Hu, D., Hu, K., Ding, D., and Liu, D.: Observed Interactions Between Black Carbon and Hydrometeor During Wet Scavenging in Mixed-Phase Clouds, *Geophys. Res. Lett.*, 46, 8453–8463, <https://doi.org/10.1029/2019GL083171>, 2019.
- Dou, T.-F. and Xiao, C.-D.: An overview of black carbon deposition and its radiative forcing over the Arctic, *Adv. Clim. Change Res.*, 7, 115–122, <https://doi.org/10.1016/j.accre.2016.10.003>, 2016.
- 540 Dupuy, R., Jourdan, O., Mioche, G., Gourbeyre, C., Leroy, D., and Schwarzenböck, A.: CDP, CIP and PIP In-situ arctic cloud microphysical properties observed during ALOUD-AC3 campaign in June 2017, <https://doi.org/10.1594/PANGAEA.899074>, 2019.
- Earle, M. E., Liu, P. S. K., Strapp, J. W., Zelenyuk, A., Imre, D., McFarquhar, G. M., Shantz, N. C., and Leaitch, W. R.:
545 Factors influencing the microphysics and radiative properties of liquid-dominated Arctic clouds: Insight from observations of aerosol and clouds during ISDAC, *J. Geophys. Res. Atmospheres*, 116, <https://doi.org/10.1029/2011JD015887>, 2011.
- Ehrlich, A., Wendisch, M., Lüpkes, C., Buschmann, M., Bozem, H., Chechin, D., Clemen, H.-C., Dupuy, R., Eppers, O., Hartmann, J., Herber, A., Jäkel, E., Järvinen, E., Jourdan, O., Kästner, U., Kliesch, L.-L., Köllner, F., Mech, M., Mertes, S., Neuber, R., Ruiz-Donoso, E., Schnaiter, M., Schneider, J., Stapf, J., and Zanatta, M.: A comprehensive in situ and remote
550 sensing data set from the Arctic CLOUD Observations Using airborne measurements during polar Day (ALOUD) campaign, *Earth Syst. Sci. Data*, 11, 1853–1881, <https://doi.org/10.5194/essd-11-1853-2019>, 2019.
- Flanner, M. G.: Arctic climate sensitivity to local black carbon, *J. Geophys. Res. Atmospheres*, 118, 1840–1851, <https://doi.org/10.1002/jgrd.50176>, 2013.

- Flanner, M. G., Zender, C. S., Hess, P. G., Mahowald, N. M., Painter, T. H., Ramanathan, V., and Rasch, P. J.: Springtime warming and reduced snow cover from carbonaceous particles, *Atmos Chem Phys*, 9, 2481–2497, <https://doi.org/10.5194/acp-9-2481-2009>, 2009.
- Gao, R. S., Schwarz, J. P., Kelly, K. K., Fahey, D. W., Watts, L. A., Thompson, T. L., Spackman, J. R., Slowik, J. G., Cross, E. S., Han, J.-H., Davidovits, P., Onasch, T. B., and Worsnop, D. R.: A Novel Method for Estimating Light-Scattering Properties of Soot Aerosols Using a Modified Single-Particle Soot Photometer, *Aerosol Sci. Technol.*, 41, 125–135, <https://doi.org/10.1080/02786820601118398>, 2007.
- Garrett, T. J., Brattström, S., Sharma, S., Worthy, D. E. J., and Novelli, P.: The role of scavenging in the seasonal transport of black carbon and sulfate to the Arctic, *Geophys. Res. Lett.*, 38, L16805, <https://doi.org/10.1029/2011GL048221>, 2011.
- Gierens, R., Kneifel, S., Shupe, M. D., Ebell, K., Maturilli, M., and Löhnert, U.: Low-level mixed-phase clouds in a complex Arctic environment, *Atmospheric Chem. Phys.*, 20, 3459–3481, <https://doi.org/10.5194/acp-20-3459-2020>, 2020.
- Gogoi, M. M., Babu, S. S., Pandey, S. K., Nair, V. S., Vaishya, A., Girach, I. A., and Koushik, N.: Scavenging ratio of black carbon in the Arctic and the Antarctic, *Polar Sci.*, <https://doi.org/10.1016/j.polar.2018.03.002>, 2018.
- Gysel, M., Laborde, M., Olfert, J. S., Subramanian, R., and Gröhn, A. J.: Effective density of Aquadag and fullerene soot black carbon reference materials used for SP2 calibration, *Atmos Meas Tech*, 4, 2851–2858, <https://doi.org/10.5194/amt-4-2851-2011>, 2011.
- Hartmann, J., Lüpkes, C., and Chechin, D.: 1Hz resolution aircraft measurements of wind and temperature during the ALOUD campaign in 2017, <https://doi.org/10.1594/PANGAEA.902849>, 2019.
- Hegg, D. A., Clarke, A. D., Doherty, S. J., and Ström4, J.: Measurements of black carbon aerosol washout ratio on Svalbard, *Tellus B Chem. Phys. Meteorol.*, 63, 891–900, <https://doi.org/10.1111/j.1600-0889.2011.00577.x>, 2011.
- Herber, A. B., Haas, C., Stone, R. S., Bottenheim, J. W., Liu, P., Li, S.-M., Staebler, R. M., Strapp, J. W., and Dethloff, K.: Regular airborne surveys of Arctic sea ice and atmosphere, *Eos Trans. Am. Geophys. Union*, 93, 41–42, <https://doi.org/10.1029/2012EO040001>, 2012.
- Hirst, E., Kaye, P. H., Greenaway, R. S., Field, P., and Johnson, D. W.: Discrimination of micrometre-sized ice and super-cooled droplets in mixed-phase cloud, *Atmos. Environ.*, 35, 33–47, [https://doi.org/10.1016/S1352-2310\(00\)00377-0](https://doi.org/10.1016/S1352-2310(00)00377-0), 2001.
- Holopainen, E., Kokkola, H., Laakso, A., and Kühn, T.: In-cloud scavenging scheme for sectional aerosol modules – implementation in the framework of the Sectional Aerosol module for Large Scale Applications version 2.0 (SALSA2.0) global aerosol module, *Geosci. Model Dev.*, 13, 6215–6235, <https://doi.org/10.5194/gmd-13-6215-2020>, 2020.
- Igel, A. L., Ekman, A. M. L., Leck, C., Tjernström, M., Savre, J., and Sedlar, J.: The free troposphere as a potential source of arctic boundary layer aerosol particles, *Geophys. Res. Lett.*, 44, 7053–7060, <https://doi.org/10.1002/2017GL073808>, 2017.
- IPCC, Masson-Delmotte, V., P. Zhai, A. Pirani, S.L., Connors, C. Péan, S. Berger, N. Caud, Y. Chen, L. Goldfarb, M.I. Gomis, M. Huang, K. Leitzell, E. Lonnoy, J.B.R., and Matthews, T.K. Maycock, T. Waterfield, O. Yelekçi, R. Yu, and B. Zhou (eds.): IPCC, 2021: Climate Change 2021: The Physical Science Basis. Contribution of Working Group I to the Sixth Assessment Report of the Intergovernmental Panel on Climate Change, 2021.

- Järvinen, E., Nehlert, F., Xu, G., Waitz, F., Mioche, G., Dupuy, R., Jourdan, O., and Schnaiter, M.: Vertical distribution of ice optical and microphysical properties in Arctic low-level mixed-phase clouds during ALOUD, *Clouds and Precipitation/Field Measurements/Troposphere/Physics (physical properties and processes)*, <https://doi.org/10.5194/acp-2022-855>, 2023.
- Jurányi, Z., Zanutta, M., Lund, M. T., Samset, B. H., Skeie, R. B., Sharma, S., Wendisch, M., and Herber, A.: Atmospheric concentrations of black carbon are substantially higher in spring than summer in the Arctic, *Commun. Earth Environ.*, 4, 1–12, <https://doi.org/10.1038/s43247-023-00749-x>, 2023.
- Kanji, Z. A., Welti, A., Corbin, J. C., and Mensah, A. A.: Black Carbon Particles Do Not Matter for Immersion Mode Ice Nucleation, *Geophys. Res. Lett.*, 47, e2019GL086764, <https://doi.org/10.1029/2019GL086764>, 2020.
- Knudsen, E. M., Heinold, B., Dahlke, S., Bozem, H., Crewell, S., Gorodetskaya, I. V., Heygster, G., Kunkel, D., Maturilli, M., Mech, M., Viceto, C., Rinke, A., Schmithüsen, H., Ehrlich, A., Macke, A., Lüpkes, C., and Wendisch, M.: Meteorological conditions during the ALOUD/PASCAL field campaign near Svalbard in early summer 2017, *Atmospheric Chem. Phys.*, 18, 17995–18022, <https://doi.org/10.5194/acp-18-17995-2018>, 2018.
- Kodros, J. K., Hanna, S. J., Bertram, A. K., Leaitch, W. R., Schulz, H., Herber, A. B., Zanutta, M., Burkart, J., Willis, M. D., Abbatt, J. P. D., and Pierce, J. R.: Size-resolved mixing state of black carbon in the Canadian high Arctic and implications for simulated direct radiative effect, *Atmospheric Chem. Phys.*, 18, 11345–11361, <https://doi.org/10.5194/acp-18-11345-2018>, 2018.
- Korolev, A., McFarquhar, G., Field, P. R., Franklin, C., Lawson, P., Wang, Z., Williams, E., Abel, S. J., Axisa, D., Borrmann, S., Crosier, J., Fugal, J., Krämer, M., Lohmann, U., Schlenker, O., Schnaiter, M., and Wendisch, M.: Mixed-Phase Clouds: Progress and Challenges, *Meteorol. Monogr.*, 58, 5.1-5.50, <https://doi.org/10.1175/AMSMONOGRAPHS-D-17-0001.1>, 2017.
- Kupc, A., Williamson, C., Wagner, N. L., Richardson, M., and Brock, C. A.: Modification, calibration, and performance of the Ultra-High Sensitivity Aerosol Spectrometer for particle size distribution and volatility measurements during the Atmospheric Tomography Mission (ATom) airborne campaign, *Atmospheric Meas. Tech.*, 11, 369–383, <https://doi.org/10.5194/amt-11-369-2018>, 2018.
- Kupiszewski, P., Zanutta, M., Mertes, S., Vochezer, P., Lloyd, G., Schneider, J., Schenk, L., Schnaiter, M., Baltensperger, U., Weingartner, E., and Gysel, M.: Ice residual properties in mixed-phase clouds at the high-alpine Jungfrauoch site, *J. Geophys. Res. Atmospheres*, 2016JD024894, <https://doi.org/10.1002/2016JD024894>, 2016.
- Laborde, M., Schnaiter, M., Linke, C., Saathoff, H., Naumann, K.-H., Möhler, O., Berlenz, S., Wagner, U., Taylor, J. W., Liu, D., Flynn, M., Allan, J. D., Coe, H., Heimerl, K., Dahlkötter, F., Weinzierl, B., Wollny, A. G., Zanutta, M., Cozic, J., Laj, P., Hittenberger, R., Schwarz, J. P., and Gysel, M.: Single Particle Soot Photometer intercomparison at the AIDA chamber, *Atmospheric Meas. Tech.*, 5, 3077–3097, <https://doi.org/10.5194/amt-5-3077-2012>, 2012.
- Laborde, M., Crippa, M., Tritscher, T., Jurányi, Z., Decarlo, P. F., Temime-Roussel, B., Marchand, N., Eckhardt, S., Stohl, A., Baltensperger, U., Prévôt, A. S. H., Weingartner, E., and Gysel, M.: Black carbon physical properties and mixing state in the European megacity Paris, *Atmos Chem Phys*, 13, 5831–5856, <https://doi.org/10.5194/acp-13-5831-2013>, 2013.

- Leaith, W. R., Korolev, A., Aliabadi, A. A., Burkart, J., Willis, M. D., Abbatt, J. P. D., Bozem, H., Hoor, P., Köllner, F., Schneider, J., Herber, A., Konrad, C., and Brauner, R.: Effects of 20–100 nm particles on liquid clouds in the cleansummertime Arctic, *Atmospheric Chem. Phys.*, 16, 11107–11124, <https://doi.org/10.5194/acp-16-11107-2016>, 2016.
- Lubin, D. and Vogelmann, A. M.: A climatologically significant aerosol longwave indirect effect in the Arctic, *Nature*, 439, 453–456, <https://doi.org/10.1038/nature04449>, 2006.
- Mahmood, R., von Salzen, K., Flanner, M., Sand, M., Langner, J., Wang, H., and Huang, L.: Seasonality of global and Arctic black carbon processes in the Arctic Monitoring and Assessment Programme models, *J. Geophys. Res. Atmospheres*, 2016JD024849, <https://doi.org/10.1002/2016JD024849>, 2016.
- McFarquhar, G. M., Ghan, S., Verlinde, J., Korolev, A., Strapp, J. W., Schmid, B., Tomlinson, J. M., Wolde, M., Brooks, S. D., Cziczo, D., Dubey, M. K., Fan, J., Flynn, C., Gultepe, I., Hubbe, J., Gilles, M. K., Laskin, A., Lawson, P., Leaith, W. R., Liu, P., Liu, X., Lubin, D., Mazzoleni, C., Macdonald, A.-M., Moffet, R. C., Morrison, H., Ovchinnikov, M., Shupe, M. D., Turner, D. D., Xie, S., Zelenyuk, A., Bae, K., Freer, M., and Glen, A.: Indirect and Semi-direct Aerosol Campaign: The Impact of Arctic Aerosols on Clouds, *Bull. Am. Meteorol. Soc.*, 92, 183–201, <https://doi.org/10.1175/2010BAMS2935.1>, 2011.
- Mertes, S., Lehmann, K., Nowak, A., Massling, A., and Wiedensohler, A.: Link between aerosol hygroscopic growth and droplet activation observed for hill-capped clouds at connected flow conditions during FEBUKO, *Atmos. Environ.*, 39, 4247–4256, <https://doi.org/10.1016/j.atmosenv.2005.02.010>, 2005.
- Mertes, S., Verheggen, B., Walter, S., Connolly, P., Ebert, M., Schneider, J., Bower, K. N., Cozic, J., Weinbruch, S., Baltensperger, U., and Weingartner, E.: Counterflow Virtual Impactor Based Collection of Small Ice Particles in Mixed-Phase Clouds for the Physico-Chemical Characterization of Tropospheric Ice Nuclei: Sampler Description and First Case Study, *Aerosol Sci. Technol.*, 41, 848–864, <https://doi.org/10.1080/02786820701501881>, 2007.
- Mioche, G., Jourdan, O., Delanoë, J., Gourbeyre, C., Febvre, G., Dupuy, R., Monier, M., Szczap, F., Schwarzenboeck, A., and Gayet, J.-F.: Vertical distribution of microphysical properties of Arctic springtime low-level mixed-phase clouds over the Greenland and Norwegian seas, *Atmospheric Chem. Phys.*, 17, 12845–12869, <https://doi.org/10.5194/acp-17-12845-2017>, 2017.
- Mori, T., Kondo, Y., Ohata, S., Zhao, Y., Sinha, P. R., Oshima, N., Matsui, H., Moteki, N., and Koike, M.: Seasonal Variation of Wet Deposition of Black Carbon in Arctic Alaska, *J. Geophys. Res. Atmospheres*, 125, e2019JD032240, <https://doi.org/10.1029/2019JD032240>, 2020.
- Morrison, H., de Boer, G., Feingold, G., Harrington, J., Shupe, M. D., and Sulia, K.: Resilience of persistent Arctic mixed-phase clouds, *Nat. Geosci.*, 5, 11–17, <https://doi.org/10.1038/ngeo1332>, 2012.
- Moteki, N. and Kondo, Y.: Dependence of Laser-Induced Incandescence on Physical Properties of Black Carbon Aerosols: Measurements and Theoretical Interpretation, *Aerosol Sci. Technol.*, 44, 663–675, <https://doi.org/10.1080/02786826.2010.484450>, 2010.
- Moteki, N., Kondo, Y., and Nakamura, S.: Method to measure refractive indices of small nonspherical particles: Application to black carbon particles, *J. Aerosol Sci.*, 41, 513–521, <https://doi.org/10.1016/j.jaerosci.2010.02.013>, 2010.

- 655 Motos, G., Schmale, J., Corbin, J. C., Modini, R. L., Karlen, N., Bertò, M., Baltensperger, U., and Gysel-Beer, M.: Cloud droplet activation properties and scavenged fraction of black carbon in liquid-phase clouds at the high-alpine research station Jungfraujoch (3580 m a.s.l.), *Atmospheric Chem. Phys.*, 19, 3833–3855, <https://doi.org/10.5194/acp-19-3833-2019>, 2019a.
- Motos, G., Schmale, J., Corbin, J. C., Zanatta, M., Baltensperger, U., and Gysel-Beer, M.: Droplet activation behaviour of
660 atmospheric black carbon particles in fog as a function of their size and mixing state, *Atmospheric Chem. Phys.*, 19, 2183–2207, <https://doi.org/10.5194/acp-19-2183-2019>, 2019b.
- Nakoudi, K., Ritter, C., Böckmann, C., Kunkel, D., Eppers, O., Rozanov, V., Mei, L., Pefanis, V., Jäkel, E., Herber, A., Maturilli, M., and Neuber, R.: Does the Intra-Arctic Modification of Long-Range Transported Aerosol Affect the Local Radiative Budget? (A Case Study), *Remote Sens.*, 12, 2112, <https://doi.org/10.3390/rs12132112>, 2020.
- 665 Neuber, R., Schmidt, L. V., Ritter, C., and Mech, M.: Cloud top altitudes observed with airborne lidar during the ACLOUD campaign, <https://doi.org/10.1594/PANGAEA.899962>, 2019.
- Noone, K. J., Ogren, J. A., Heintzenberg, J., Charlson, R. J., and Covert, D. S.: Design and Calibration of a Counterflow Virtual Impactor for Sampling of Atmospheric Fog and Cloud Droplets, *Aerosol Sci. Technol.*, 8, 235–244, <https://doi.org/10.1080/02786828808959186>, 1988.
- 670 Ogren, J. A., Heintzenberg, J., and Charlson, R. J.: In-situ sampling of clouds with a droplet to aerosol converter, *Geophys Res Lett*, 12, 121–124, <https://doi.org/10.1029/GL012i003p00121>, 1985.
- Ohata, S., Schwarz, J. P., Moteki, N., Koike, M., Takami, A., and Kondo, Y.: Hygroscopicity of materials internally mixed with black carbon measured in Tokyo, *J. Geophys. Res. Atmospheres*, 121, 2015JD024153, <https://doi.org/10.1002/2015JD024153>, 2016.
- 675 Ohata, S., Koike, M., Yoshida, A., Moteki, N., Adachi, K., Oshima, N., Matsui, H., Eppers, O., Bozem, H., Zanatta, M., and Herber, A. B.: Arctic black carbon during PAMARCMiP 2018 and previous aircraft experiments in spring, *Atmospheric Chem. Phys.*, 21, 15861–15881, <https://doi.org/10.5194/acp-21-15861-2021>, 2021.
- Oshima, N., Yukimoto, S., Deushi, M., Koshiro, T., Kawai, H., Tanaka, T. Y., and Yoshida, K.: Global and Arctic effective radiative forcing of anthropogenic gases and aerosols in MRI-ESM2.0, *Prog. Earth Planet. Sci.*, 7, 38,
680 <https://doi.org/10.1186/s40645-020-00348-w>, 2020.
- Petzold, A., Onasch, T., Kebejian, P., and Freedman, A.: Intercomparison of a Cavity Attenuated Phase Shift-based extinction monitor (CAPS PMex) with an integrating nephelometer and a filter-based absorption monitor, *Atmos Meas Tech*, 6, 1141–1151, <https://doi.org/10.5194/amt-6-1141-2013>, 2013.
- Quinn, P. K., Stohl, A., Arnold, S., Baklanov, A., Berntsen, T. K., Christensen, J. H., Eckhardt, S., Flanner, M., Klimont, Z.,
685 Korsholm, U. S., and others: AMAP Assessment 2015: Black carbon and ozone as Arctic climate forcers, 2015.
- Raatikainen, T., Brus, D., Hyvärinen, A.-P., Svensson, J., Asmi, E., and Lihavainen, H.: Black carbon concentrations and mixing state in the Finnish Arctic, *Atmos Chem Phys*, 15, 10057–10070, <https://doi.org/10.5194/acp-15-10057-2015>, 2015.

- Roiger, A., Thomas, J.-L., Schlager, H., Law, K. S., Kim, J., Schäfler, A., Weinzierl, B., Dahlkötter, F., Krisch, I., Marelle, L., Minikin, A., Raut, J.-C., Reiter, A., Rose, M., Scheibe, M., Stock, P., Baumann, R., Bouarar, I., Clerbaux, C., George, M., Onishi, T., and Flemming, J.: Quantifying Emerging Local Anthropogenic Emissions in the Arctic Region: The ACCESS Aircraft Campaign Experiment, *Bull. Am. Meteorol. Soc.*, 96, 441–460, <https://doi.org/10.1175/BAMS-D-13-00169.1>, 2015.
- 690 Samset, B. H., Myhre, G., Schulz, M., Balkanski, Y., Bauer, S., Berntsen, T. K., Bian, H., Bellouin, N., Diehl, T., Easter, R. C., Ghan, S. J., Iversen, T., Kinne, S., Kirkevåg, A., Lamarque, J.-F., Lin, G., Liu, X., Penner, J. E., Seland, Ø., Skeie, R. B., Stier, P., Takemura, T., Tsigaridis, K., and Zhang, K.: Black carbon vertical profiles strongly affect its radiative forcing uncertainty, *Atmos Chem Phys*, 13, 2423–2434, <https://doi.org/10.5194/acp-13-2423-2013>, 2013.
- 695 Samset, B. H., Stjern, C. W., Andrews, E., Kahn, R. A., Myhre, G., Schulz, M., and Schuster, G. L.: Aerosol Absorption: Progress Towards Global and Regional Constraints, *Curr. Clim. Change Rep.*, 4, 65–83, <https://doi.org/10.1007/s40641-018-0091-4>, 2018.
- Sand, M., Berntsen, T. K., Kay, J. E., Lamarque, J. F., Seland, Ø., and Kirkevåg, A.: The Arctic response to remote and local forcing of black carbon, *Atmos Chem Phys*, 13, 211–224, <https://doi.org/10.5194/acp-13-211-2013>, 2013.
- 700 Schnaiter, M. and Järvinen, E.: SID-3 1Hz size distribution of cloud particles during the ACLOUD campaign in 2017, <https://doi.org/10.1594/PANGAEA.900261>, 2019.
- Schroder, J. C., Hanna, S. J., Modini, R. L., Corrigan, A. L., Kreidenwies, S. M., Macdonald, A. M., Noone, K. J., Russell, L. M., Leaitch, W. R., and Bertram, A. K.: Size-resolved observations of refractory black carbon particles in cloud droplets at a marine boundary layer site, *Atmos Chem Phys*, 15, 1367–1383, <https://doi.org/10.5194/acp-15-1367-2015>, 2015.
- 705 Schulz, H., Zanatta, M., Bozem, H., Leaitch, W. R., Herber, A. B., Burkart, J., Willis, M. D., Kunkel, D., Hoor, P. M., Abbatt, J. P. D., and Gerdes, R.: High Arctic aircraft measurements characterising black carbon vertical variability in spring and summer, *Atmospheric Chem. Phys.*, 19, 2361–2384, <https://doi.org/10.5194/acp-19-2361-2019>, 2019.
- Schwarz, J. P., Gao, R. S., Fahey, D. W., Thomson, D. S., Watts, L. A., Wilson, J. C., Reeves, J. M., Darbeheshti, M., Baumgardner, D. G., Kok, G. L., Chung, S. H., Schulz, M., Hendricks, J., Lauer, A., Kärcher, B., Slowik, J. G., Rosenlof, K. H., Thompson, T. L., Langford, A. O., Loewenstein, M., and Aikin, K. C.: Single-particle measurements of midlatitude black carbon and light-scattering aerosols from the boundary layer to the lower stratosphere, *J. Geophys. Res. Atmospheres*, 111, D16207, <https://doi.org/10.1029/2006JD007076>, 2006.
- 710 Schwarz, J. P., Samset, B. H., Perring, A. E., Spackman, J. R., Gao, R. S., Stier, P., Schulz, M., Moore, F. L., Ray, E. A., and Fahey, D. W.: Global-scale seasonally resolved black carbon vertical profiles over the Pacific, *Geophys. Res. Lett.*, 40, 2013GL057775, <https://doi.org/10.1002/2013GL057775>, 2013.
- Schwarz, J. P., Perring, A. E., Markovic, M. Z., Gao, R. S., Ohata, S., Langridge, J., Law, D., McLaughlin, R., and Fahey, D. W.: Technique and theoretical approach for quantifying the hygroscopicity of black-carbon-containing aerosol using a single particle soot photometer, *J. Aerosol Sci.*, 81, 110–126, <https://doi.org/10.1016/j.jaerosci.2014.11.009>, 2015.
- 720 Sedlar, J., Shupe, M. D., and Tjernström, M.: On the Relationship between Thermodynamic Structure and Cloud Top, and Its Climate Significance in the Arctic, *J. Clim.*, 25, 2374–2393, <https://doi.org/10.1175/JCLI-D-11-00186.1>, 2011.

- Shupe, M. D. and Intrieri, J. M.: Cloud Radiative Forcing of the Arctic Surface: The Influence of Cloud Properties, Surface Albedo, and Solar Zenith Angle, *J. Clim.*, 17, 616–628, [https://doi.org/10.1175/1520-0442\(2004\)017<0616:CRFOTA>2.0.CO;2](https://doi.org/10.1175/1520-0442(2004)017<0616:CRFOTA>2.0.CO;2), 2004.
- 725 Shupe, M. D., Persson, P. O. G., Brooks, I. M., Tjernström, M., Sedlar, J., Mauritsen, T., Sjogren, S., and Leck, C.: Cloud and boundary layer interactions over the Arctic sea ice in late summer, *Atmospheric Chem. Phys.*, 13, 9379–9399, <https://doi.org/10.5194/acp-13-9379-2013>, 2013.
- Solomon, A., Feingold, G., and Shupe, M. D.: The role of ice nuclei recycling in the maintenance of cloud ice in Arctic mixed-phase stratocumulus, *Atmospheric Chem. Phys.*, 15, 10631–10643, <https://doi.org/10.5194/acp-15-10631-2015>, 2015.
- 730 Stachlewska, I. S.: Investigation of tropospheric arctic aerosol and mixed-phase clouds using airborne lidar technique, Universität Potsdam, 2005.
- Stachlewska, I. S., Neuber, R., Lampert, A., Ritter, C., and Wehrle, G.: AMALi – the Airborne Mobile Aerosol Lidar for Arctic research, *Atmospheric Chem. Phys.*, 10, 2947–2963, <https://doi.org/10.5194/acp-10-2947-2010>, 2010.
- Stephens, M., Turner, N., and Sandberg, J.: Particle identification by laser-induced incandescence in a solid-state laser cavity, *Appl. Opt.*, 42, 3726–3736, <https://doi.org/10.1364/AO.42.003726>, 2003.
- 735 Taketani, F., Miyakawa, T., Takashima, H., Komazaki, Y., Kanaya, Y., Taketani, F., Miyakawa, T., Inoue, J., Kanaya, Y., Takashima, H., Pan, X., and Inoue, J.: Ship-borne observations of atmospheric black carbon aerosol particles over the Arctic Ocean, Bering Sea, and North Pacific Ocean during September 2014, *J. Geophys. Res. Atmospheres*, 2015JD023648, <https://doi.org/10.1002/2015JD023648>, 2016.
- 740 Tørseth, K., Andrews, E., Asmi, E., Eleftheriadis, K., Fiebig, M., Herber, A., Huang, L., Kylling, A., Lupi, A., Massling, A., Mazzola, M., Nøjgaard, J. K., Popovicheva, O., Schichtel, B., Schmale, J., Sharma, S., Skov, H., Stebel, K., Vassel, B., Vitale, V., Whaley, C., Yttri, K. E., and Zannata, M.: Review of Observation Capacities and Data Availability for Black Carbon in the Arctic Region: EU Action on Black Carbon in the Arctic – Technical Report 1, 2019.
- Vochezer, P., Järvinen, E., Wagner, R., Kupiszewski, P., Leisner, T., and Schnaiter, M.: In situ characterization of mixed phase clouds using the Small Ice Detector and the Particle Phase Discriminator, *Atmospheric Meas. Tech.*, 9, 159–177, <https://doi.org/10.5194/amt-9-159-2016>, 2016.
- 745 Wendisch, M., Macke, A., Ehrlich, A., Lüpkes, C., Mech, M., Chechin, D., Dethloff, K., Velasco, C. B., Bozem, H., Brückner, M., Clemen, H.-C., Crewell, S., Donth, T., Dupuy, R., Ebell, K., Egerer, U., Engelmann, R., Engler, C., Eppers, O., Gehrman, M., Gong, X., Gottschalk, M., Gourbeyre, C., Griesche, H., Hartmann, J., Hartmann, M., Heinold, B., Herber, A., Herrmann, H., Heygster, G., Hoor, P., Jafariserajehlou, S., Jäkel, E., Järvinen, E., Jourdan, O., Kästner, U., Kecorius, S., Knudsen, E. M., Köllner, F., Kretschmar, J., Lelli, L., Leroy, D., Maturilli, M., Mei, L., Mertes, S., Mioche, G., Neuber, R., Nicolaus, M., Nomokonova, T., Notholt, J., Palm, M., van Pinxteren, M., Quaas, J., Richter, P., Ruiz-Donoso, E., Schäfer, M., Schmieder, K., Schnaiter, M., Schneider, J., Schwarzenböck, A., Seifert, P., Shupe, M. D., Siebert, H., Spreen, G., Stapf, J., Stratmann, F., Vogl, T., Welti, A., Wex, H., Wiedensohler, A., Zannata, M., and Zeppenfeld, S.: The Arctic Cloud Puzzle: Using

- 755 ACLOUD/PASCAL Multiplatform Observations to Unravel the Role of Clouds and Aerosol Particles in Arctic Amplification, *Bull. Am. Meteorol. Soc.*, 100, 841–871, <https://doi.org/10.1175/BAMS-D-18-0072.1>, 2018.
- Wendisch, M., Brückner, M., Crewell, S., Ehrlich, A., Notholt, J., Lüpkes, C., Macke, A., Burrows, J. P., Rinke, A., Quaas, J., Maturilli, M., Schemann, V., Shupe, M. D., Akansu, E. F., Barrientos-Velasco, C., Bärfuss, K., Blechschmidt, A.-M., Block, K., Bougoudis, I., Bozem, H., Böckmann, C., Bracher, A., Bresson, H., Bretschneider, L., Buschmann, M., Chechin, D. G.,
- 760 Chylik, J., Dahlke, S., Deneke, H., Dethloff, K., Donth, T., Dorn, W., Dupuy, R., Ebell, K., Egerer, U., Engelmann, R., Eppers, O., Gerdes, R., Gierens, R., Gorodetskaya, I. V., Gottschalk, M., Griesche, H., Gryanik, V. M., Handorf, D., Harm-Altstädter, B., Hartmann, J., Hartmann, M., Heinold, B., Herber, A., Herrmann, H., Heygster, G., Höschel, I., Hofmann, Z., Hölemann, J., Hünerbein, A., Jafariserajehlou, S., Jäkel, E., Jacobi, C., Janout, M., Jansen, F., Jourdan, O., Jurányi, Z., Kalesse-Los, H., Kanzow, T., Käßner, R., Kliesch, L. L., Klingebiel, M., Knudsen, E. M., Kovács, T., Körtke, W., Krampe, D., Kretzschmar,
- 765 J., Kreyling, D., Kulla, B., Kunkel, D., Lampert, A., Lauer, M., Lelli, L., Lerber, A. von, Linke, O., Löhnert, U., Lonardi, M., Losa, S. N., Losch, M., Maahn, M., Mech, M., Mei, L., Mertes, S., Metzner, E., Mewes, D., Michaelis, J., Mioche, G., Moser, M., Nakoudi, K., Neggens, R., Neuber, R., Nomokonova, T., Oelker, J., Papakonstantinou-Presvelou, I., et al.: Atmospheric and Surface Processes, and Feedback Mechanisms Determining Arctic Amplification: A Review of First Results and Prospects of the (AC)3 Project, *Bull. Am. Meteorol. Soc.*, 1, <https://doi.org/10.1175/BAMS-D-21-0218.1>, 2022.
- 770 Wesche, C., Steinhage, D., and Nixdorf, U.: Polar aircraft Polar5 and Polar6 operated by the Alfred Wegener Institute, *J. Large-Scale Res. Facil. JLSRF*, 2, 87, <https://doi.org/10.17815/jlsrf-2-153>, 2016.
- Whaley, C. H., Mahmood, R., von Salzen, K., Winter, B., Eckhardt, S., Arnold, S., Beagley, S., Becagli, S., Chien, R.-Y., Christensen, J., Damani, S. M., Dong, X., Eleftheriadis, K., Evangeliou, N., Faluvegi, G., Flanner, M., Fu, J. S., Gauss, M., Giardi, F., Gong, W., Hjorth, J. L., Huang, L., Im, U., Kanaya, Y., Krishnan, S., Klimont, Z., Kühn, T., Langner, J., Law, K.
- 775 S., Marelle, L., Massling, A., Olivie, D., Onishi, T., Oshima, N., Peng, Y., Plummer, D. A., Popovicheva, O., Pozzoli, L., Raut, J.-C., Sand, M., Saunders, L. N., Schmale, J., Sharma, S., Skeie, R. B., Skov, H., Taketani, F., Thomas, M. A., Traversi, R., Tsigaridis, K., Tsyro, S., Turnock, S., Vitale, V., Walker, K. A., Wang, M., Watson-Parris, D., and Weiss-Gibbons, T.: Model evaluation of short-lived climate forcings for the Arctic Monitoring and Assessment Programme: a multi-species, multi-model study, *Atmospheric Chem. Phys.*, 22, 5775–5828, <https://doi.org/10.5194/acp-22-5775-2022>, 2022.
- 780 Xu, J.-W., Martin, R. V., Morrow, A., Sharma, S., Huang, L., Leaitch, W. R., Burkart, J., Schulz, H., Zanatta, M., Willis, M. D., Henze, D. K., Lee, C. J., Herber, A. B., and Abbatt, J. P. D.: Source attribution of Arctic black carbon constrained by aircraft and surface measurements, *Atmospheric Chem. Phys.*, 17, 11971–11989, <https://doi.org/10.5194/acp-17-11971-2017>, 2017.
- Yoshida, A., Moteki, N., Ohata, S., Mori, T., Tada, R., Dagsson-Waldhauserová, P., and Kondo, Y.: Detection of light-absorbing iron oxide particles using a modified single-particle soot photometer, *Aerosol Sci. Technol.*, 50, 1–4, <https://doi.org/10.1080/02786826.2016.1146402>, 2016.

- Yoshida, A., Moteki, N., Ohata, S., Mori, T., Koike, M., Kondo, Y., Matsui, H., Oshima, N., Takami, A., and Kita, K.: Abundances and Microphysical Properties of Light-Absorbing Iron Oxide and Black Carbon Aerosols Over East Asia and the Arctic, *J. Geophys. Res. Atmospheres*, 125, e2019JD032301, <https://doi.org/10.1029/2019JD032301>, 2020.
- 790 Yuan, J., Modini, R. L., Zanatta, M., Herber, A. B., Müller, T., Wehner, B., Poulain, L., Tuch, T., Baltensperger, U., and Gysel-Beer, M.: Variability in the mass absorption cross section of black carbon (BC) aerosols is driven by BC internal mixing state at a central European background site (Melpitz, Germany) in winter, *Atmospheric Chem. Phys.*, 21, 635–655, <https://doi.org/10.5194/acp-21-635-2021>, 2021.
- Zanatta, M. and Herber, A.: Aircraft measurements of aerosol size distribution in the Arctic during the ACLOUD campaign
795 2017, <https://doi.org/10.1594/PANGAEA.900341>, 2019a.
- Zanatta, M. and Herber, A.: Aircraft measurements of refractory black carbon in the Arctic during the ACLOUD campaign
2017, <https://doi.org/10.1594/PANGAEA.899937>, 2019b.
- Zanatta, M., Laj, P., Gysel, M., Baltensperger, U., Vratolis, S., Eleftheriadis, K., Kondo, Y., Dubuisson, P., Winiarek, V., Kazadzis, S., Tunved, P., and Jacobi, H.-W.: Effects of mixing state on optical and radiative properties of black carbon in the
800 European Arctic, *Atmospheric Chem. Phys.*, 18, 14037–14057, <https://doi.org/10.5194/acp-18-14037-2018>, 2018.
- Zanatta, M., Bozem, H., Köllner, F., Schneider, J., Kunkel, D., Hoor, P., Faria, J. de, Petzold, A., Bundke, U., Hayden, K., Staebler, R. M., Schulz, H., and Herber, A. B.: Airborne survey of trace gases and aerosols over the Southern Baltic Sea: from clean marine boundary layer to shipping corridor effect, *Tellus B Chem. Phys. Meteorol.*, 72, 1–24, <https://doi.org/10.1080/16000889.2019.1695349>, 2020.

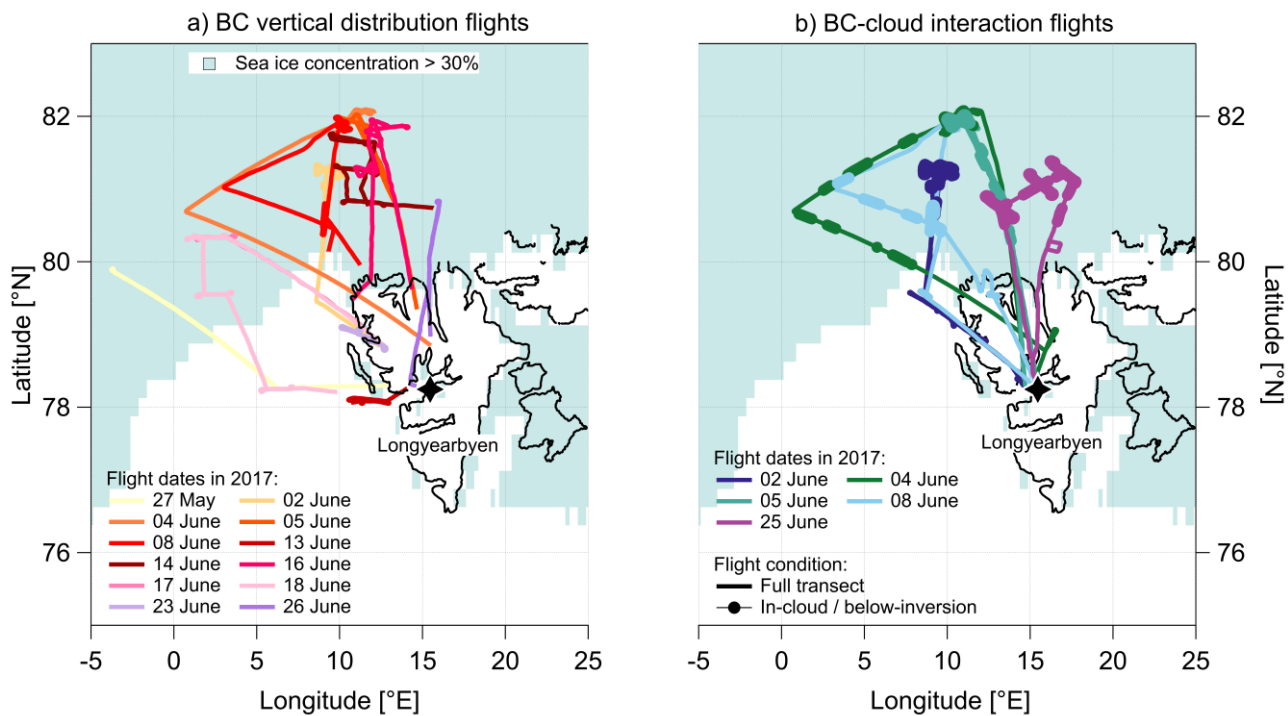
805

Tables

810 **Table 1** List of atmospheric variables observed and computed in this study, including meteorology, aerosol particles (AP), black carbon particles (BC) and cloud particles.

Variable	Symbol	Unit	Instrument	Inlet	Aircraft	Size range (diameter)
Meteorology						
Temperature	T	°C	-	-	P6	-
Potential temperature	T_P	K	-	-	P6	-
Relative humidity	RH	%	-	-	P6	-
Aerosol particles, AP						
AP number concentration	N_{AP}	cm ⁻³	UHSAS	Total	P6	80-1000 nm
AP residuals number concentration	N_{AP-res}	cm ⁻³	UHSAS	CVI	P6	80-1000 nm
Black carbon particles, BC						
BC mass concentration	M_{BC}	ng m ⁻³	SP2	Total	P6	73-575 nm
BC number concentration	N_{BC}	cm ⁻³	SP2	Total	P6	73-575 nm
BC mass-equivalent diameter	D_{BC}	nm	SP2	Total & CVI	P6	73-575 nm
BC geometric mean diameter	D_{BC-Geo}	nm	SP2	Total & CVI	P6	73-575 nm
BC modal diameter	D_{BC-Mod}	nm	SP2	Total & CVI	P6	73-575 nm
BC residual mass concentration	M_{BC-res}	ng m ⁻³	SP2	CVI	P6	73-575 nm
BC residuals number concentration	N_{BC-res}	cm ⁻³	SP2	CVI	P6	73-575 nm
Cloud particles						
Droplet number concentration	N_{Dro}	cm ⁻³	SID-3	-	P6	5-45 μm
Droplet number concentration, $D > 10 \mu\text{m}$	N_{Dro10}	cm ⁻³	SID-3	-	P6	10-45 μm
Liquid water content	LWC	g m ⁻³	SID-3	-	P6	5-45 μm
Ice water content	IWC	g m ⁻³	CIP	-	P6	75-1550 μm
Ice water fraction	IWF	-	CIP - SID-3	-	P6	5-1550 μm
Clout top height	-	m asl	AMALi	-	P5	-

Figures



815

Figure 1 Map of Svalbard including flight patterns of the Polar 6 aircraft in May-June 2017 for the flights dedicated to investigating the vertical distribution (a) and cloud interaction (b) of BC particles. Sea ice concentration was derived from the GHRST Sea Surface Temperature Level 4, MUR25 sea surface temperature analysis product with 0.25° resolution (MUR-JPL-L4-GLOB-v4.1 doi:10.5067/GHGMR-4FJ04).

820

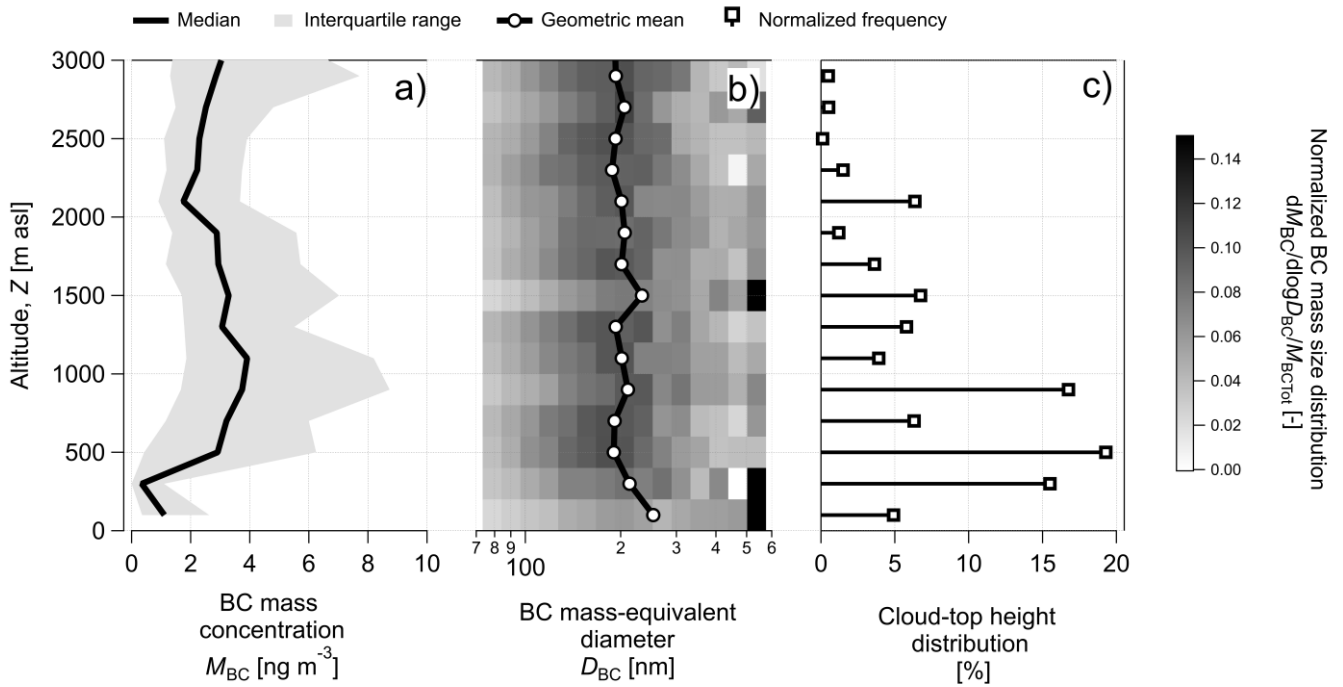


Figure 2 Vertical variability of: a) BC mass concentration; b) BC mass size distribution; c) cloud top height. BC particles were sampled via the total inlet and measured with the SP2 in the 73-575 nm diameter range. Cloud top was derived from the AMALI instrument. Statistics were calculated for equidistant altitude steps starting at the surface (0m asl) and being 100m thick.

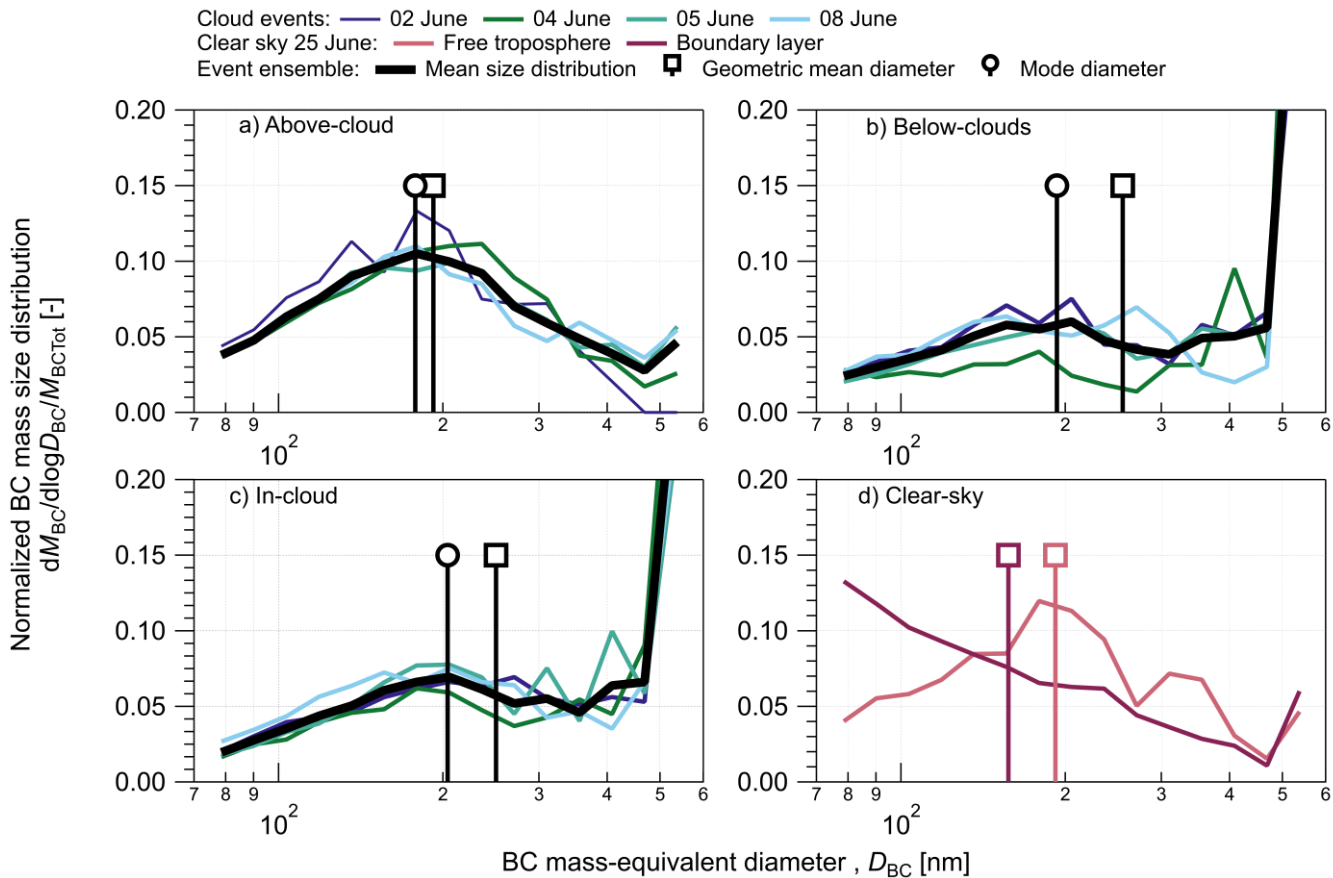
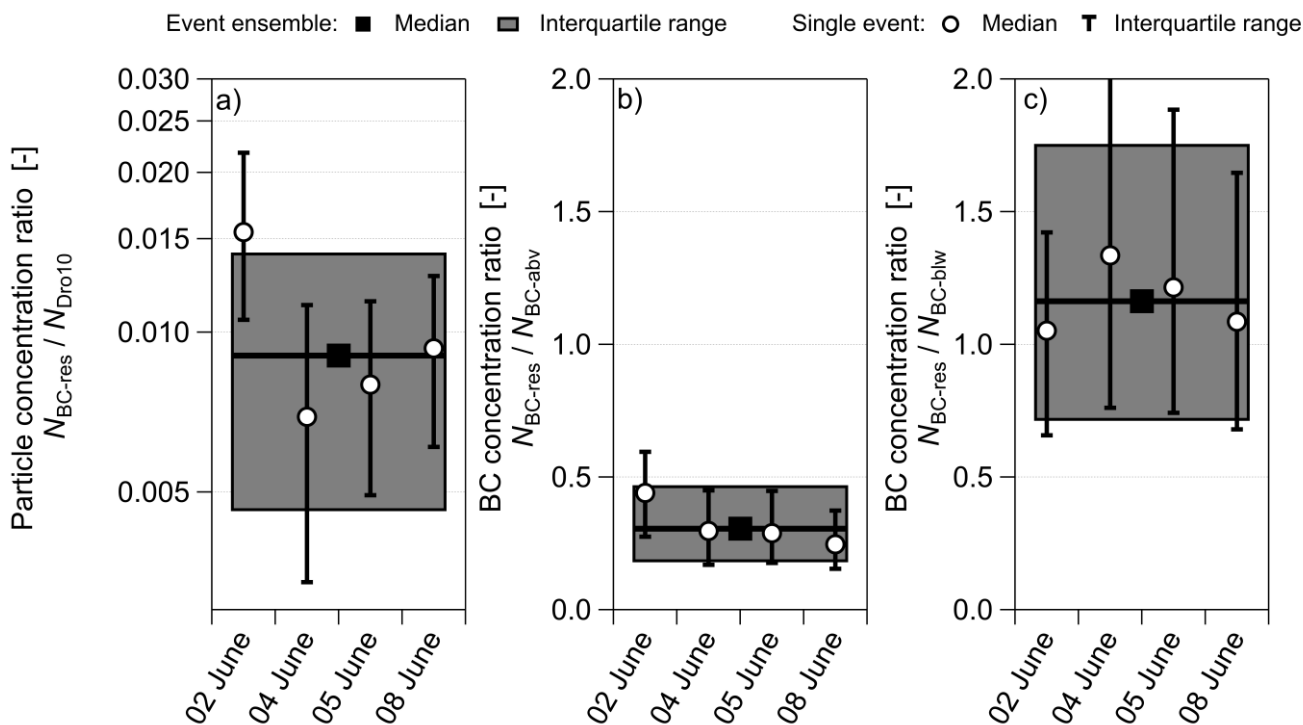
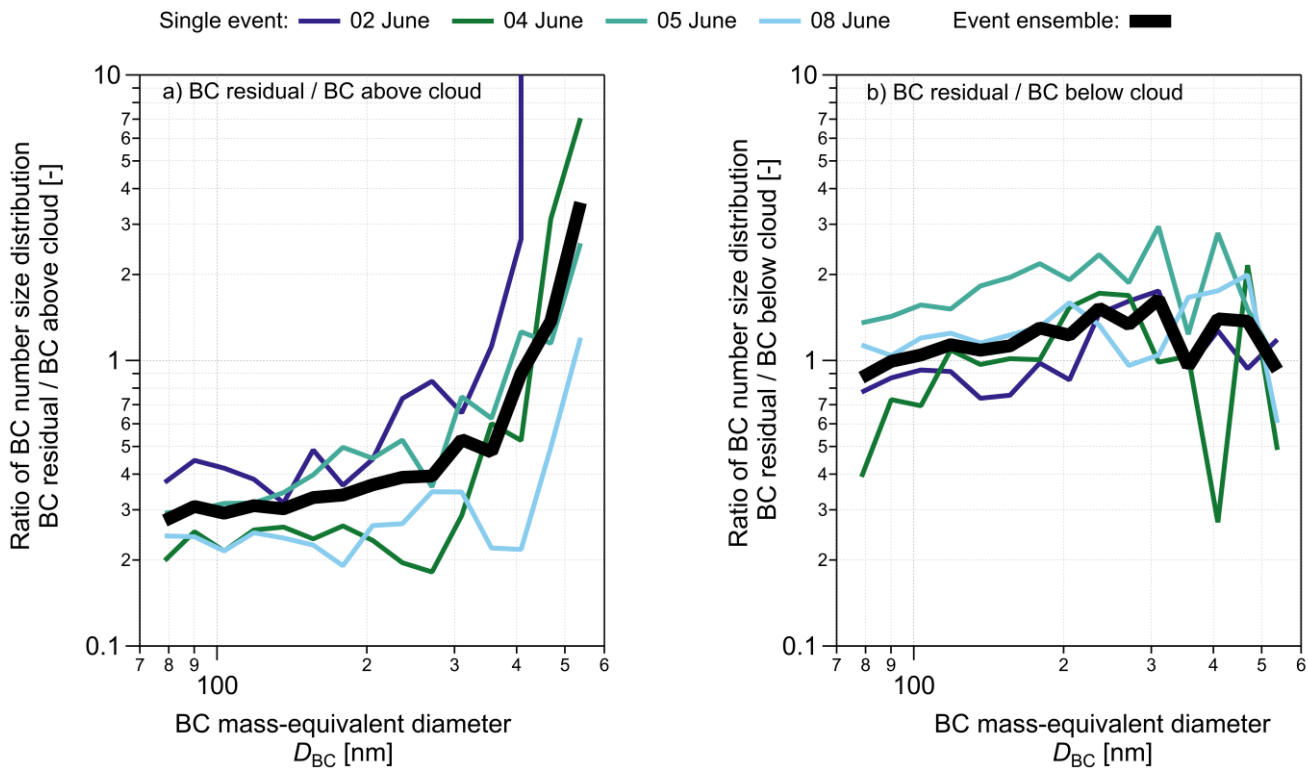


Figure 3 BC normalized mass size distribution observed in: a) above cloud; b) below clouds; c) in cloud; d) clear sky. BC residuals were sampled via the CVI inlet, while BC particles were sampled via the total inlet. Both BC residuals and BC particles were measured with the SP2 in the 73-575 nm diameter range.

830

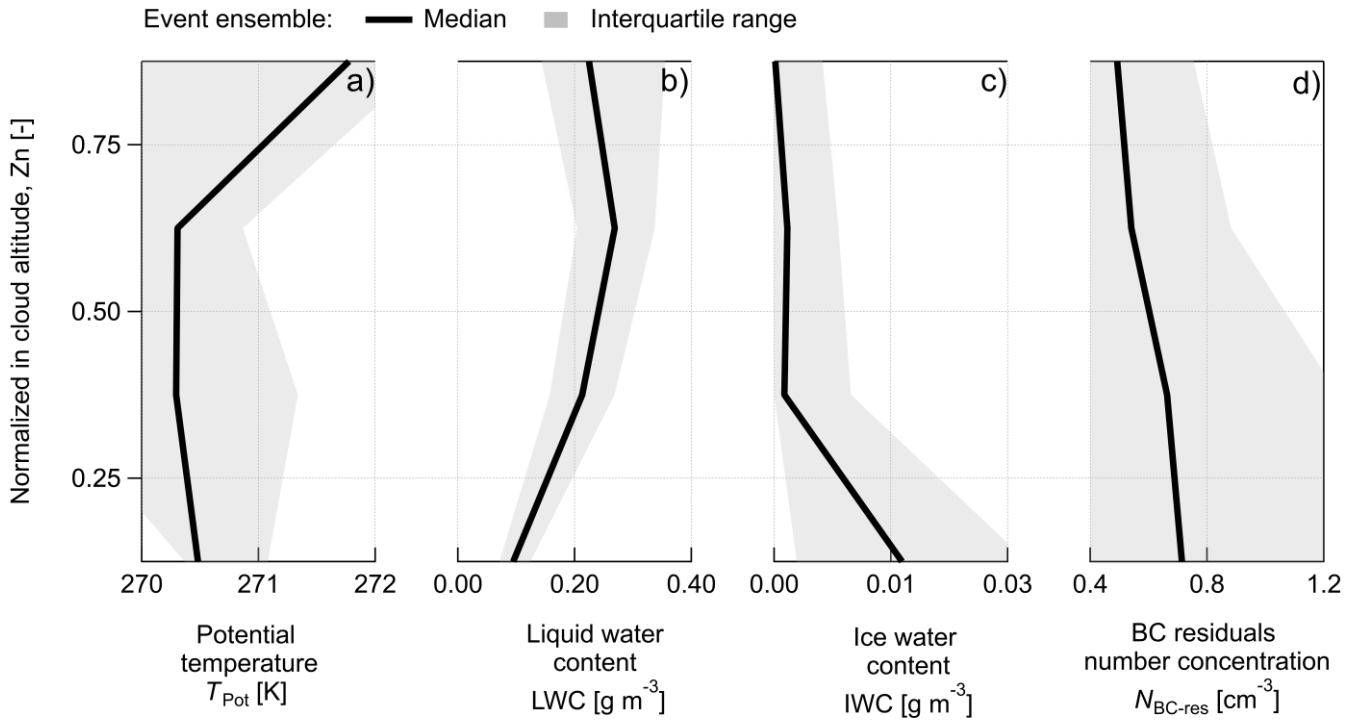


835 **Figure 4** Box-plot of BC concentration in cloud residuals: a) Ratio between the number concentration of cloud residuals (N_{BC-res}) and the liquid droplet number concentration (N_{Dro10}); b) Ratio between the number concentration of cloud residuals (N_{BC-res}) and the number concentration of BC particles measured above cloud (N_{BC-abv}); c) Ratio between the number concentration of cloud residuals (N_{BC-res}) and the number concentration of BC particles measured below cloud (N_{BC-blw}). Liquid droplets were measured with the SID-3 probe in the 10-45 μm diameter range. BC residuals were sampled via the CVI inlet, while BC particles were sampled via the total inlet. Both BC residuals and BC particles were measured with the SP2 in the 73-575 nm diameter range.



840

Figure 5 Ratio of number size distribution of BC residuals over number size distribution of BC particles sampled above cloud (a) and below cloud (b). BC residuals were sampled via the CVI inlet, while BC particles were sampled via the total inlet. Both BC residuals and BC particles were measured with the SP2 in the 73-575 nm diameter range.



845

Figure 6 Vertical profiles of the cloud ensemble: a) Potential temperature, T_{Pot} ; b) Liquid water content, LWC; c) Ice water content, IWC; d) BC residual number concentration, N_{BC-res} . Median and interquartile range were calculated for equidistant normalized altitude (Z_n) steps of 0.25. Liquid droplets were measured with the SID-3 probe in the 5-45 μm diameter range. Ice crystals were measured with the CIP probe in the 75-1550 μm diameter range. BC residuals were sampled via the CVI inlet and measured with the SP2 in the 73-575 nm diameter range.

850

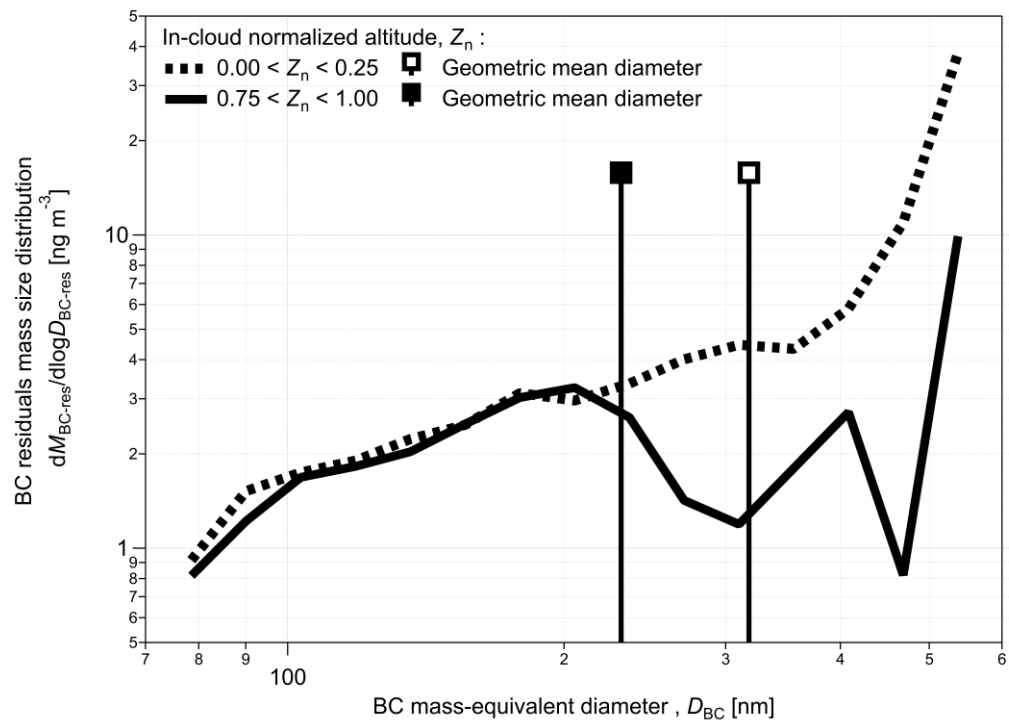


Figure 7 Mass size distribution of BC residuals measured at the cloud top (0.75 < Z_n < 1.00) and cloud-bottom (0.00 < Z_n < 0.25). BC residuals were sampled via the CVI inlet and measured with the SP2 in the 73-575 nm diameter range.